A&A 560, A41 (2013)
DOI: 10.1051/0004-6361/201322129


Astronomy & Astrophysics

# Gas-phase CO depletion and $N_2H^+$ abundances in starless cores⋆,⋆⋆

N. Lippok[1], R. Launhardt[1], D. Semenov[1], A. M. Stutz[1], Z. Balog[1], Th. Henning[1], O. Krause[1], H. Linz[1], M. Nielbock[1], Ya. N. Pavlyuchenkov[2], M. Schmalzl[3], A. Schmiedeke[4], and J. H. Bieging[5]

[1] Max-Planck-Institut für Astronomie (MPIA), Königstuhl 17, 69117 Heidelberg, Germany
e-mail: lippok@mpia.de
[2] Institute of Astronomy, Russian Academy of Sciences, Pyatnitskaya str. 48, 119017 Moscow, Russia
[3] Leiden Observatory, Leiden University, PO Box 9513, 2300 RA Leiden, The Netherlands
[4] Universität zu Köln, Zülpicher Str. 77, 50937 Köln, Germany
[5] Department of Astronomy and Steward Observatory, University of Arizona, Tucson AZ 85721, USA

Received 24 June 2013 / Accepted 13 September 2013

**ABSTRACT**

*Context.* In the dense and cold interiors of starless molecular cloud cores, a number of chemical processes allow for the formation of complex molecules and the deposition of ice layers on dust grains. Dust density and temperature maps of starless cores derived from *Herschel* continuum observations constrain the physical structure of the cloud cores better than ever before. We use these to model the temporal chemical evolution of starless cores.

*Aims.* We derive molecular abundance profiles for a sample of starless cores. We then analyze these using chemical modeling based on dust temperature and hydrogen density maps derived from *Herschel* continuum observations.

*Methods.* We observed the $^{12}$CO (2–1), $^{13}$CO (2–1), C$^{18}$O (2–1) and $N_2H^+$ (1–0) transitions towards seven isolated, nearby low-mass starless molecular cloud cores. Using far infrared (FIR) and submillimeter (submm) dust emission maps from the *Herschel* key program Earliest Phases of Star formation (EPoS) and by applying a ray-tracing technique, we derived the physical structure (density, dust temperature) of these cores. Based on these results we applied time-dependent chemical modeling of the molecular abundances. We modeled the molecular emission profiles with a line-radiative transfer code and compared them to the observed emission profiles.

*Results.* CO is frozen onto the grains in the center of all cores in our sample. The level of CO depletion increases with hydrogen density and ranges from 46% up to more than 95% in the core centers of the three cores with the highest hydrogen density. The average hydrogen density at which 50% of CO is frozen onto the grains is $1.1 \pm 0.4 \times 10^5$ cm$^{-3}$. At about this density, the cores typically have the highest relative abundance of $N_2H^+$. The cores with higher central densities show depletion of $N_2H^+$ at levels of 13% to 55%. The chemical ages for the individual species are on average $(2 \pm 1) \times 10^5$ yr for $^{13}$CO, $(6 \pm 3) \times 10^4$ yr for C$^{18}$O, and $(9 \pm 2) \times 10^4$ yr for $N_2H^+$. Chemical modeling indirectly suggests that the gas and dust temperatures decouple in the envelopes and that the dust grains are not yet significantly coagulated.

*Conclusions.* We observationally confirm chemical models of CO-freezeout and nitrogen chemistry. We find clear correlations between the hydrogen density and CO depletion and the emergence of $N_2H^+$. The chemical ages indicate a core lifetime of less than 1 Myr.

**Key words.** astrochemistry – ISM: abundances – submillimeter: ISM – infrared: ISM – stars: formation – stars: low-mass

## 1. Introduction

Stars form in cold cloud cores. In the prestellar phase, the centers of the cloud cores cool down to temperatures below 10 K and the hydrogen densities typically exceed $10^5$ cm$^{-3}$. In these conditions complex molecules are synthesized (Bacmann et al. 2012). At the same time, in the densest regions of the cores, many molecular species stick onto the dust grains (e.g., Bergin & Tafalla 2007). The evolution of the chemical composition influences the cooling rate of the clouds and changes the degree of ionization, both important properties that influence the star formation process.

The gas in the local interstellar medium (ISM) consists of 98% molecular hydrogen and helium. These species, however, do not emit at cold temperatures. Therefore, CO has become a popular tracer of the ISM. It is the second most abundant molecule and readily excited already at low temperatures. However, in the conditions in prestellar cores, CO freezes out onto the dust grains. This alters the chemical composition of the cloud cores and the dust properties. Nitrogen-bearing species like $N_2H^+$, which are otherwise destroyed by CO molecules, can now accumulate in the gas phase and trace these denser regions. $N_2H^+$ molecules form and deplete on longer time scales than does CO. Under reasonable assumptions of the initial abundances, physical conditions, and reaction rates, modeling both species together can therefore constrain the chemical age of the cores.

While early studies had already detected CO mantles on dust grains from absorption features in the mid-infrared (e.g., Tielens et al. 1991), direct observational proof of molecular depletion from the gas phase in the centers of dense cores came only later.

⋆ This work is partially based on observations by the *Herschel* Space Observatory. *Herschel* is an ESA space observatory with science instruments provided by European-led Principal Investigator consortia and with important participation from NASA.

⋆⋆ Appendices are available in electronic form at http://www.aanda.org

**Table 1.** Source list.

| Source | Other names | RA, Dec (J2000)[a] [h:m:s, °:′:″] | Region | Dist. [pc] | Ref. |
|---|---|---|---|---|---|
| CB 4 | ... | 00:39:05.2, +52:51:47 | Cas A, Gould Belt (GB) | 350 ± 150 | 1 |
| CB 17[b] | L 1389 | 04:04:37.1, +56:56:02 | Perseus, GB | 250 ± 50 | 2, 1 |
| CB 26[c] | L 1439 | 05:00:14.5, +52:05:59 | Taurus-Auriga | 140 ± 20 | 2, 3,4 |
| CB 27 | L 1512 | 05:04:08.1, +32:43:30 | Taurus-Auriga | 140 ± 20 | 3, 4, 5 |
| B68 | L 57, CB 82 | 17:22:38.3, –23:49:51 | Ophiuchus, Pipe nebula | 135 ± 15 | 6, 7, 8 |
| CB 130[d] | L 507 | 18:16:14.3, –02:32:41 | Aquila rift, GB | 250 ± 50 | 9, 10 |
| CB 244[e] | L 1262 | 23:25:26.8, +74:18:22 | Cepheus flare, GB | 200 ± 30 | 2, 4, 11 |

**Notes.** [(a)] Positions of the center of the starless cores, defined as the column density peaks found in Launhardt et al. (2013). [(b)] CB 17: additional low-luminosity Class I YSO 25″ from the starless core. [(c)] CB 26: additional Class I YSO 3.6′ southwest of the starless core. [(d)] CB 130: additional Class 0 core ∼30″ east and Class I YSO ∼45″ east of starless core. [(e)] CB 244: additional Class 0 source ∼90″ east of the starless core.

**References.** (1) Perrot & Grenier (2003); (2) Launhardt et al. (2010); (3) Loinard et al. (2011); (4) Stutz et al. (2009); (5) Launhardt et al. (2013); (6) de Geus et al. (1989); (7) Lombardi et al. (2006); (8) Alves & Franco (2007); (9) Launhardt & Henning (1997); (10) Straižys et al. (2003); (11) Kun (1998).

It requires the accurate determination of molecular abundances in the gas phase and of the total gas mass. One of the most robust ways to determine the total mass in dense clouds is to infer it via a presumably known gas-to-dust mass ratio from (column-) densities of the dust. They in turn can be derived from the black-body radiation of the dust grains (e.g., Launhardt et al. 2013) or the visual to mid-infrared extinction caused by the dust (e.g., Witt et al. 1990; Alves et al. 2001).

Several studies have been performed that quantify the CO depletion in starless cores on the basis of hydrogen masses deduced from dust measurements (e.g., Willacy et al. 1998; Caselli et al. 1999; Bacmann et al. 2002; Bergin et al. 2002; Tafalla et al. 2004; Pagani et al. 2005; Stutz et al. 2009; Ford & Shirley 2011). All of them find strong indications of a central freezeout of CO. So far, however, the observational studies of molecular depletion have only had weak constraints on the temperature distribution within molecular clouds or none at all. Knowledge of the dust temperature is, however, essential for both derivation of column densities from the dust emission and robust chemical modeling (Pavlyuchenkov et al. 2007). Uncertainties in the temperature also introduce large errors into the hydrogen densities derived from (sub-)mm dust emission.

Isolated Bok globules, which often contain only a single dense core and are devoid of larger envelopes, are the best suited objects for detailed studies of the physical and chemical structure of starless cores. We therefore observed seven globules containing a starless core as part of the *Herschel* guaranteed time key project Earliest Phases of Star formation (EPoS). The *Herschel* Space Observatory (Pilbratt et al. 2010) and its sensitive PACS (Poglitsch et al. 2010) and SPIRE (Griffin et al. 2010) bolometer arrays have made it possible to sample the peak of the thermal spectral energy distributions (SED) of cold molecular clouds with high sensitivity and spatial resolution for the first time. In Stutz et al. (2010); Launhardt et al. (2013) we presented dust temperature and hydrogen density maps of the starless cores in the globules derived by modified black-body fits to the continuum emission. We also developed a ray-tracing method to restore the full volume density and dust temperature structure of these cores. The results are presented in Nielbock et al. (2012) for B 68, for CB 17 in Schmalzl et al. (2013), and in this paper for the remaining five globules.

We also present maps of the $^{12}$CO ($J$ = 2−1), $^{13}$CO ($J$ = 2−1), C$^{18}$O ($J$ = 2−1), and $N_2H^+$ ($J$ = 1−0) transitions of the same seven globules. The maps of $^{12}$CO ($J$ = 2−1) and $^{13}$CO ($J$ = 2−1) of globules CB 17, CB 26, and CB 244 were previously presented in Stutz et al. (2009). Based on dust temperature and hydrogen density maps derived from the *Herschel* observations, and using time-dependent chemical modeling, we derive the molecular abundances. From the modeling results, we also constrain the chemical age of the cores and infer information on the dust grains in the globules.

The paper is structured as follows. In Sect. 2 we describe the observations and data reduction. In Sect. 3 we describe our modeling approaches. In Sect. 4 we present and discuss the results. We summarize our findings in Sect. 5. Maps of the observations and the derived dust density and hydrogen density maps are shown in Appendix B. We also present a simple local thermodynamical equilibrium (LTE) analysis of the molecular column densities in Appendix C.

## 2. Observations

### 2.1. Source selection

Within the EPoS project, 12 nearby Bok globules have been observed with the *Herschel* bolometers. The sample of globules has been selected based on results from previous studies (see Launhardt et al. 2013, and references therein) and was known to contain low-mass pre- and proto-stellar cores. Of particular importance for the selection was the criterion that the globules be very isolated and located outside the galactic plane. Their mean galactic latitude is 7.3 ± 3 degrees, with the closest one still 3.5 degrees away from the galactic plane, such that background levels and confusion from the galactic plane are minimized. Out of the 12 globules, seven globules contain starless cores. These globules are studied in this paper and are listed in Table 1. Three of the globules contain only a single starless core (CB 4, CB 27, and B 68), one contains an additional Class 0 core (CB 244), and two contain an additional Class I young stellar object (CB 17 and CB 26). CB 130 contains two additional cores (Class 0 and I).

### 2.2. Continuum observations

All globules were observed in the *Herschel* PACS bands at 100 and 160 $\mu$m and the *Herschel* SPIRE bands at 250 $\mu$m, 350 $\mu$m, and 500 $\mu$m. These observations were complemented with ground-based (sub-)mm observations ranging from 450 $\mu$m to 1.2 mm. The respective observations and data reduction are described in detail in Nielbock et al. (2012) and Launhardt et al. (2013), and references therein. The dust temperature and

**Table 2.** List of observations.

| Source | Line | Freq. [GHz] | Tel. | Date [mo/yr] | *HPBW* [arcsec] | $\Delta v$ [m s$^{-1}$] | $\eta_{mb}$ | Map size | Ref. |
|---|---|---|---|---|---|---|---|---|---|
| CB 4 | $^{12}$CO (2–1) | 230.537990 | HHT | 10/09 | 32.2 | 300 | 0.85 | 10′ × 10′ | |
| | $^{13}$CO (2–1) | 220.398686 | HHT | 10/09 | 33.7 | 300 | 0.85 | 10′× 10′ | |
| | C$^{18}$O (2–1) | 219.560319 | 30 m | 12/10 | 11.3 | 53 | 0.52 | 3′× 3′ | |
| | $N_2H^+$ (1–0) | 93.1737 | 30 m | 12/10 | 26.6 | 63 | 0.75 | 3′ × 3′ | |
| CB 17 | $^{12}$CO (2–1) | 230.537990 | HHT | 04/08 | 32.2 | 300 | 0.85 | 10′ × 10′ | |
| | $^{13}$CO (2–1) | 220.398686 | HHT | 04/08 | 33.7 | 300 | 0.85 | 10′ × 10′ | |
| | C$^{18}$O (2–1) | 219.560319 | 30 m | 10/96 | 10.9 | 107 | 0.48 | 35″/ 7″ | |
| | $N_2H^+$ (1–0) | 93.1737 | 30 m | 10/96 | 26.6 | 63 | 0.95 | 140″ × 140″ | |
| CB 26 | $^{12}$CO (2–1) | 230.537990 | HHT | 03/09 | 32.2 | 300 | 0.85 | 10′ × 10′ | 1 |
| | $^{13}$CO (2–1) | 220.398686 | HHT | 03/09 | 33.7 | 300 | 0.85 | 10′ × 10′ | 1 |
| | C$^{18}$O (2–1) | 219.560319 | 30m | 12/10 | 11.3 | 53 | 0.52 | 6′ × 5′ | |
| | $N_2H^+$ (1–0) | 93.1737 | 30m | 12/10 | 26.6 | 63 | 0.75 | 6′ × 5′ | |
| CB 27 | $^{12}$CO (2–1) | 230.537990 | HHT | 01/07 | 32.2 | 300 | 0.85 | 10′ × 10′ | 1 |
| | $^{13}$CO (2–1) | 220.398686 | HHT | 01/07 | 33.7 | 300 | 0.85 | 10′ × 10′ | 1 |
| | C$^{18}$O (2–1) | 219.560319 | 30 m | 12/10 | 11.3 | 53 | 0.52 | 3′ × 3′ | |
| | $N_2H^+$ (1–0) | 93.1737 | 30 m | 12/10 | 26.6 | 63 | 0.75 | 3′ × 3′ | |
| B 68 | $^{12}$CO (2–1) | 230.537990 | HHT | 03/08 | 32.2 | 300 | 0.85 | 10′ × 10′ | |
| | $^{13}$CO (2–1) | 220.398686 | HHT | 03/08 | 33.7 | 300 | 0.85 | 10′ × 10′ | |
| | C$^{18}$O (1–0) | 109.782182 | 30 m | 04/00 | 23.6 | 30 | 0.91 | 4′ × 4′/ 12″[a] | |
| | $N_2H^+$ (1–0) | 93.1737 | 30 m | 04/01 | 26.6 | 63 | 0.75 | 3′ × 3′/ 12–24″[a] | |
| CB 130 | $^{12}$CO (2–1) | 230.537990 | 30 m | 07/11 | 11.3 | 51 | 0.92 | 4′ × 4′ | |
| | $^{13}$CO (2–1) | 220.398686 | 30 m | 07/11 | 11.8 | 53 | 0.92 | 4′ × 3′ | |
| | C$^{18}$O (2–1) | 219.560319 | 30 m | 01/11 | 11.3 | 53 | 0.52 | 5′ × 5′ | |
| | $N_2H^+$ (1–0) | 93.1737 | 30 m | 01/11 | 26.6 | 63 | 0.75 | 5′ × 5′ | |
| CB 244 | $^{12}$CO (2–1) | 230.537990 | HHT | 04/08 | 32.2 | 300 | 0.85 | 10′ × 10′ | 1 |
| | $^{13}$CO (2–1) | 220.398686 | HHT | 04/08 | 33.7 | 300 | 0.85 | 10′ × 10′ | 1 |
| | C$^{18}$O (2–1) | 219.560319 | 30 m | 12/10 | 11.3 | 53 | 0.52 | 5′ × 5′ | |
| | $N_2H^+$ (1–0) | 93.1737 | 30 m | 12/10 | 26.6 | 63 | 0.75 | 5′ × 5′ | |

**Notes.** [(a)] Data first presented in Bergin et al. (2002). These maps were obtained from tracked observations with the listed pointing separations.

**References.** (1) Stutz et al. (2009).

density maps presented in Sect. 4.1 were derived from this set of observations.

### 2.3. Molecular line observations

On-the-fly maps of the C$^{18}$O ($J$ = 2–1) line at 219.560 GHz and the $N_2H^+$ ($J$ = 1–0) line complex around 93.174 GHz were taken at the IRAM 30m telescope between November 2010 and January 2011 of all starless cores except B 68. For this globule, we used data that were obtained before and published in Bergin et al. (2002). The observing parameters are compiled in Table 2. Map sizes are different for different sources and range from 3′×3′ to 6′×5′. The HPBWs were 12″ for C$^{18}$O and 28″ for $N_2H^+$. The channel widths were 40 kHz for C$^{18}$O and 20 kHz for $N_2H^+$, corresponding to 0.05 and 0.06 km s$^{-1}$. Both molecular transitions were observed simultaneously using the EMIR receivers (Carter et al. 2012). Calibration was done using the standard chopper-wheel method every 15 min. The weather conditions were mixed during the course of the observations leading to mean system temperatures of 700 K for C$^{18}$O and 180 K for $N_2H^+$. During the observations of CB 130, the weather was better, resulting in lower system temperatures of 300 K and 100 K.

To minimize scanning artifacts, the on-the-fly maps were taken with two orthogonal scan directions with two coverages each and a scanning speed of 6″/s. A reference position was observed approximately every 1.5 min. These positions were derived from IRIS 100 $\mu$m all-sky maps (Miville-Deschênes & Lagache 2005). They lie within extended regions of the lowest 100 $\mu$m continuum emission, preferably within 10′ from the source, and were expected to have no CO emission.

Molecular line maps of the $^{12}$CO and $^{13}$CO species at the $J$ = 2–1 transition (230.538 GHz and 220.399 GHz) were obtained with the *Heinrich Hertz* Submilimeter Telescope (HHT) on Mt. Graham, Arizona, USA. The channel width was ~0.34 km s$^{-1}$ and the angular resolution of the telescope was 32″ (FWHM). For more details on the observations and data reduction, we refer the reader to Stutz et al. (2009).

Table 2 lists all molecular line observations used for this study. All maps were reprojected to the coordinate system of the corresponding dust temperature and density maps. They have also been smoothed to the same Gaussian beam size of 36.4″ (resolution of the SPIRE 500 $\mu$m maps and the dust temperature and density maps) and been regridded to the same pixel scale of 10″ × 10″.

## 3. Modeling

### 3.1. Dust temperature and density maps from ray-tracing models

The goal of the ray-tracing fitting of the continuum observations of the starless cores is to go beyond the line-of-sight (LoS) optical depth-averaged analysis presented in Launhardt et al. (2013)

by also modeling the dust temperature variation along the LoS and deriving volume density distributions. The ray-tracing algorithm developed to derive the dust temperature and density structure of the cores from the *Herschel* and complementary ground-based continuum maps is described in Nielbock et al. (2012). Here, we only briefly summarize the hydrogen density and temperature profiles used by the algorithm and mention the formulae to illustrate the meaning of the profile parameters.

For all modeling steps we use the dust opacities $\kappa_{\rm d}(\nu)$ tabulated in Ossenkopf & Henning (1994)[1] for mildly coagulated composite dust grains with thin ice mantles ($10^5$ yrs coagulation time at gas density $10^5\,{\rm cm}^{-3}$)[2]. The density profiles of the cores have been modeled assuming a "Plummer"-like shape (Plummer 1911), which characterizes the radial density distribution of prestellar cores on the verge of gravitational collapse (Whitworth & Ward-Thompson 2001):

$$n_{\rm H}(r) = \frac{\Delta n}{\left(1+\left(\frac{r}{r_0}\right)^2\right)^{\eta/2}} + n_{\rm out} \quad \text{if } r \le r_{\rm out} \tag{1}$$

where $n_{\rm H} = 2\times n({\rm H_2}) + n({\rm H})$ is the total number density of hydrogen nuclei. The radius $r_{\rm out}$ sets the outer boundary of the model cloud. The density beyond this radius is set to zero. We add a constant term to the profile to account for the fact that the outer density and column density profiles in most globules do not drop off like a power law, but turn over into a low-density envelope. This profile (i) accounts for an inner flat density core inside $r_0$ with a peak density $n_0 = n_{\rm out} + \Delta n$ ($\Delta n \gg n_{\rm out}$), (ii) approaches modified power-law behavior with an exponent $\eta$ at $r \gg r_0$, (iii) turns over into a flat-density halo outside $r_1$, where

$$r_1 = r_0\sqrt{\left(\frac{\Delta n}{n_{\rm out}}\right)^{2/\eta} - 1}\,, \tag{2}$$

and (iv) is cut off at $r_{\rm out}$. The tenuous envelope is actually neither azimuthally symmetric nor fully spatially recovered by our observations. Therefore, its real size remains unconstrained, and $r_{\rm out}$ cannot be considered a reliable source property.

For the temperature profile of an externally heated cloud, we adopt the following empirical prescription. It resembles the radiation transfer equation in coupling the local temperature to the effective optical depth toward the outer "rim", where the interstellar radiation field (ISRF) affects

$$T(r) = T_{\rm out} - \Delta T\left(1 - {\rm e}^{-\tau(r)}\right) \tag{3}$$

with $\Delta T = T_{\rm out} - T_{\rm in}$ and the frequency-averaged effective optical depth

$$\tau(r) = \tau_0\frac{\int_r^{r_{\rm out}} n_{\rm H}(x)\,{\rm d}x}{\int_0^{r_{\rm out}} n_{\rm H}(x)\,{\rm d}x}. \tag{4}$$

Here, $\tau_0$ is an empirical (i.e., free) scaling parameter that accounts for the a priori unknown mean dust opacity and the SED of the UV radiation of the ISRF, and $T_{\rm in}$ is the minimum, inner temperature and is determined by IR and cosmic ray heating.

The results of this modeling approach are presented in Sect. 4.1. The uncertainties of the method have been discussed thoroughly in Nielbock et al. (2012) and Launhardt et al. (2013). They come to the conclusion that the largest uncertainty (up to a factor 3) in the derived density is introduced by the uncertainty in the dust opacities. Additional uncertainties are introduced by the assumed distances, the gas-to-dust ratio, the symmetry assumption (w.r.t. the plane-of-sky) for the LoS, and the limited angular resolution. In particular, in the center of the cores, the density can be systematically underestimated due to beam smoothing. We therefore estimate the overall fitting uncertainty of the derived density maps to be ±25%, plus a scaling uncertainty by up to a factor 3 due to the not well-constrained dust opacity model. The accuracy of the dust temperature is not as strongly affected by these effects and the modeled dust temperature has an estimated uncertainty of $^{+2}_{-1}$ K.

### 3.2. Chemical modeling

On the basis of the dust temperature and the hydrogen density maps that were derived using the ray-tracing technique and that are presented in Sect. 4.1, we model the chemical evolution of the molecular gas in the cloud cores. The density and temperature profiles are kept constant during the chemical evolution of the cores. The gas is initially atomic, comprising 13 elements, and it evolves with time because of the processes described below. This approach of a chemical evolution under constant physical conditions is often called "pseudo time-dependent". We call the time span during which the chemical models evolve "chemical age". How this parameter is related to the "real" age of the cores is discussed in Sect. 4.4.4.

We act on the assumption that the gas temperature is equal to the dust temperature everywhere in the clouds. This simplifying assumption should hold to first order at hydrogen densities above $10^4\,{\rm cm}^{-3}$ where dust and gas are collisionally coupled (Galli et al. 2002) and where most of the molecular emission originates. However, the coupling might not be perfect even in the densest regions of our study ($>10^6\,{\rm cm}^{-3}$): for example, for B 68, where we have derived a central hydrogen density of $4\times10^5\,{\rm cm}^{-3}$ and central dust temperature of 8 K, Hotzel et al. (2002) and Lai et al. (2003) find a central gas temperature of 10−11 K from ammonia observations. On the other hand, ammonia might be depleted in the core center such that it instead traces a somewhat warmer inner layer of the envelope. In our model of B 68, the dust temperature in a shell of radius 5000 to 7000 AU is indeed 10−11 K. This could also explain at least part of this small discrepancy. The decoupling of gas and dust temperatures at lower densities affects our modeling results less than the chemical evolution, since the rotational transitions at low densities are subthermally excited. For instance, at a hydrogen density of $10^3\,{\rm cm}^{-3}$ and a gas temperature of 100 K, the $J = 2$–1 transition of CO would only be excited to about 9 K, while the same transition would be excited to 5 K at a gas temperature of 20 K[3]. Therefore, underestimating the gas temperature affects the modeled level populations and the molecular emission at low densities only weakly.

In the vicinity of the core centers, the majority of globules show almost circularly symmetric shapes. As we study these central cloud regions, the modeling is performed assuming 1D radial profiles. We obtain 1D profiles of the observed molecular emission and the dust temperature and density maps by azimuthal averaging. We cut out the segment of the circle in the direction of asymmetries for the averaging task. The regions that have been taken into account for deriving the 1D profiles are indicated in Figs. A.1–A.7. The resulting profiles of the

[1] ftp://cdsarc.u-strasbg.fr/pub/cats/J/A+A/291/943

[2] This is not identical to the often-used OH5 opacities, which were calculated for a gas density of $10^6\,{\rm cm}^{-3}$.

[3] This has been calculated using the online version of RADEX (van der Tak et al. 2007).

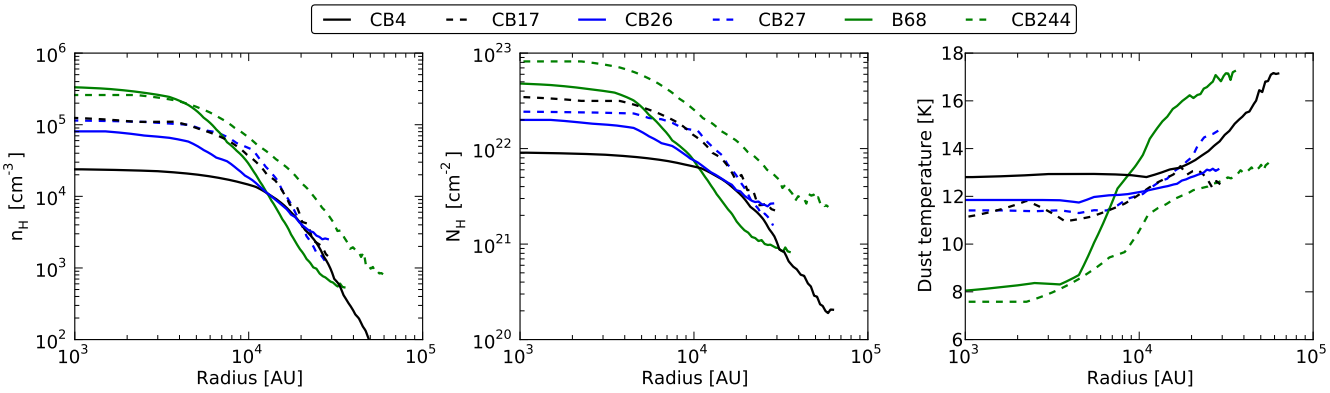


**Fig. 1.** Azimuthally averaged profiles of the hydrogen density (*left*), hydrogen column density (*center*), and dust temperature (*right*) derived with the ray-tracing technique.

dust temperature, hydrogen densities, and column densities are shown in Fig. 1.

We use the time-dependent gas-grain chemical model "ALCHEMIC" (see Semenov et al. 2010). A brief summary is given below. The chemical network is based on the 2007 version of the OSU network[4]. The reaction rates as of November 2010 are implemented (e.g., from the KIDA database[5]). We consider cosmic ray particles (CRP) and CRP-induced secondary UV photons as the only external ionizing sources. We adopt a CRP ionization rate of $\zeta_{\rm CR} = 1.3 \times 10^{-17}$ s$^{-1}$ (Herbst & Klemperer 1973), although recent studies have revealed higher CRP ionization rates in translucent clouds (e.g., Indriolo et al. 2012). The dense molecular cloud cores studied here are embedded in extended envelopes that, despite their low density, effectively scatter the low energy particles of the cosmic rays and thereby reduce the luminosity of the cosmic rays in the shielded regions. Therefore the lower value of Herbst & Klemperer (1973) is expected to hold for dense and shielded clouds (e.g., Garrod 2013; Vasyunin & Herbst 2013). The UV dissociation and ionization photo rates are adopted from van Dishoeck et al. (2006)[6]. The self-shielding of $H_2$ from photodissociation is calculated by Eq. (37) from Draine & Bertoldi (1996). The shielding of CO by dust grains, $H_2$, and its self-shielding are calculated using the precomputed table of Lee et al. (1996, Table 11). As the chemical model does not include carbon isotopologues, the self-shielding factors for $^{12}C^{18}O$ are calculated by lowering the $^{12}C^{16}O$ abundances by an appropriate isotopic ratio (see below).

In addition to gas-phase chemistry, the chemical model includes the following gas-grain interaction processes. (We refer the reader to Sect. 2.3 in Semenov et al. 2010, for the corresponding equations.) Molecules accrete on and stick to dust grains by physisorption with 100% probability, except for $H_2$, which is not allowed to stick. Chemisorption of surface molecules is not allowed. The surface molecules are released back to the gas phase by thermal, CRP-, and CRP-induced UV-photodesorption. All these processes are modeled with a first-order kinetics approach (Eq. (2) in Semenov et al. 2010). A UV photodesorption yield for surface species of $10^{-3}$ is assumed (e.g., Öberg et al. 2009a,b). The grain charging is modeled by dissociative recombination and radiative neutralization of ions on grains, and by electron sticking to grains. The synthesis of complex molecules is included, using a set of surface reactions and photoprocessing of ices from Garrod & Herbst (2006). We assume that each 0.1 $\mu$m spherical olivine grain provides $\approx 1.88 \times 10^6$ surface sites for accreting gaseous species (Biham et al. 2001). The surface recombination proceeds only via the Langmuir-Hinshelwood mechanism. Upon a surface recombination, the reaction products are assumed to remain on the grains. Following Katz et al. (1999), we use the standard rate equation approach to the surface chemistry and do not consider tunneling of H and $H_2$ through the grain surface.

Overall, our chemical network consists of 656 species made of 13 elements and 7907 reactions. All chemical parameters are kept fixed during the iterative fitting of the observational data. With this model we calculate time-dependent CO and $N_2H^+$ abundances and use them for the line radiative transfer modeling and fitting of the observed spectral maps.

In the cloud 1D physical model, the density profiles are cut off at an outer radius where either no density could be derived because the continuum emission is too weak or where the morphology of the cloud becomes asymmetric. These radii are also the outer boundaries for the chemical modeling. At these radii the density has, however, not yet dropped to zero as the cores are further embedded in low-density extended envelopes. We therefore have to take into account that the external UV field is already attenuated at the outer edge of the cores. We derive the extinction level by converting the column density at the outer boundaries to an extinction level $A_V$. We use a conversion factor $A_v/N_{\rm H}$ of $1 \times 10^{-21}$ cm$^2$. This is the average value estimated by comparing the $N_{\rm H}$ maps derived from the dust emission to complementary near-infrared extinction maps (see Launhardt et al. 2013; Kainulainen et al. 2006), which will be presented and discussed in more detail in a forthcoming paper.

We want to compare models and observations of $^{13}CO$, $C^{18}O$, and $N_2H^+$. Since the rare isotopologues are not explicitly taken into account in the chemical modeling, we proceed in two steps. In the first step, we calculate the chemical model for $^{12}CO$ to get the $N_2H^+$ abundances accurately. The modeling itself also consists of two steps. First, the abundance of the molecules and the corresponding shielding factors are calculated using an analytic approximation. The shielding factors are subsequently used for the second step, the full time-dependent modeling. To calculate the profiles of $^{13}CO$ and $C^{18}O$, we artificially decrease the $^{12}CO$ abundance by a factor in the analytic approximation and calculate the shielding-factor for these species. They are used for the time-dependent chemical modeling. The initial abundances are, however, taken to be the same as for the modeling of $^{12}CO$.

[4] see: http://www.physics.ohio-state.edu/~eric/research.html
[5] http://kida.obs.u-bordeaux1.fr
[6] http://www.strw.leidenuniv.nl/~ewine/photo/

**Table 3.** Parameters of the hydrogen density and dust temperature profiles corresponding to Eqs. (1)–(4).

| Source | $N_0$[a] [cm$^{-2}$] | $n_0$[a] [cm$^{-3}$] | $n_{out}$ [$10^2$cm$^{-3}$] | $\eta$[b] | $r_0$ [$10^4$ AU] | $r_1$ [$10^4$ AU] | $r_{out}$ [$10^4$ AU] | $T_{in}$[c] [K] | $T_{out}$[c] [K] |
|---|---|---|---|---|---|---|---|---|---|
| CB 4 | $9.2\times10^{21}$ | $2.5\times10^{4}$ | 1 | 5.0 | 2.0 | 5.7 | 8 | 13.1 | 19 |
| CB 17[d] | $3.0\times10^{22}$ | $1.3\times10^{5}$ | 6 | 5.0 | 1.1 | 3.0 | 4 | 10.5 | 13 |
| CB 26 | $2.0\times10^{22}$ | $8.7\times10^{4}$ | 5 | 3.0 | 0.8 | 4.4 | 3 | 12.0 | 14 |
| CB 27 | $2.7\times10^{22}$ | $1.3\times10^{5}$ | 7 | 6.0 | 1.3 | 6.6 | 3 | 11.3 | 14 |
| B 68[d] | $5.5\times10^{22}$ | $4.0\times10^{5}$ | 4 | 5.0 | 0.7 | 2.7 | 5 | 8.1 | 17 |
| CB 244 | $9.1\times10^{22}$ | $2.5\times10^{5}$ | 7 | 4.0 | 1.1 | 4.7 | 7 | 8.4 | 14 |

**Notes.** [(a)] The estimated relative uncertainty is ±25%, plus a scaling uncertainty by up to a factor of 3 due to the not well-constrained dust opacity model (see uncertainty discussion in Sect. 3.1.). [(b)] The estimated uncertainty is ±1. [(c)] The estimated uncertainty is ±1 K. The temperature estimate is less affected by the dust model (see Launhardt et al. 2013). [(d)] Slight differences to the values derived by Schmalzl et al. (2013) and Nielbock et al. (2012) can be accounted to the uncertainties discussed in Sect. 3.1.

To obtain the abundance of the rare isotopologues, the resulting abundances of the time-dependent modeling are divided by the corresponding fraction of these species with respect to their main isotopologue. This approach allows us to take the reduced self-shielding of $^{13}$CO and C$^{18}$O into account with respect to $^{12}$CO without extending the chemical network to the rarer isotopologues. In the literature there is a spread of values mentioned for the ratios of the isotopologues. We use a fraction of 1/70 for $^{13}$CO with respect to $^{12}$CO and 1/490 for C$^{18}$O (Wilson & Rood 1994; Lodders et al. 2009).

Since the temperature and abundances of the molecules vary along the LoS, the molecular emission could be partly subthermally excited or be optically thick. For these reasons, we calculate the rotational level populations and emission of the molecules from the synthetic abundance profiles using line-radiative transfer modeling. It is not our goal to model the kinematics of the cores. For the pure purpose of modeling the line-shape and the total intensity of the transitions, we can neglect variations of macroscopic and turbulent motions in the cores, since they are so weak that this simplification does not affect the results for the molecular abundances. We use the non-LTE line radiative transfer code "LIME" (Brinch & Hogerheijde 2010) and the molecular data files of the "Leiden Atomic and Molecular Database" (Schöier et al. 2005). The LIME code allows to take into account line-broadening due to micro turbulent motions. This is done by setting a scalar Doppler broadening parameter. Since the linewidths in the globules do not vary significantly over the globules, it is possible to set this parameter such that the linewidths of models and observations agree everywhere. The Doppler broadening parameter is taken as one free parameter in the modeling process. In this way we ensure that the optical depth of the emission is properly taken into account. The macroscopic velocity field in the modeling is set to zero. The velocity channel width is set to the value of the observed spectral cubes and the pixel spacing is set to 10″ to which all observational data are also regridded.

For the comparison of synthetic and observed spectra, the latter have been prepared as follows. We have removed line shifts from macroscopic motions in the observed spectra since we do not model the kinetics of the cores. For this task, the spectra have been fitted and shifted by the derived $v_{LSR}$ such that the centers of all spectra are located at $v_{LSR} = 0$. They have also been rebinned such that $v_{LSR} = 0$ lies in the center of a bin as is the case for the synthetic spectra. Finally, the spectra are azimuthally averaged. The resulting radially varying spectra build up the reference to which the modeled spectra can be compared directly.

During the course of the modeling, we vary four parameters. The chemical model has only one "true" free parameter, the chemical age, which is the time during which the gas evolves at constant physical conditions. In addition, we take into account uncertainties in the derived hydrogen densities of up to a factor 3 resulting from the uncertainties of the assumed dust properties (see Sect. 3.1). The relative initial abundances of the atomic species are kept constant when the hydrogen density is varied. We also need to consider that the hydrogen density has not dropped to zero at the outer boundaries of the model cores. Halos of dust particles around the globules with a mean extinction $A_V$ of typically 1−3 mag are detected in the SPIRE, as well as NIR extinction maps that are quite extended. Since these envelopes shield the globules from the UV-part of the ISRF, they need to be considered in the chemical modeling. The halos are not strictly spherically symmetric, either in extinction / column density or in extent, as pointed out in Launhardt et al. (2013). To account for this and other uncertainties discussed in Sect. 4.4.5, we consider the measured mean envelope extinction as a starting guess only and vary them during the modeling procedure.

We find the best model in the following way. The relative differences of observed and synthetic spectra are summed up for each velocity bin and at all radii. The model with the lowest value of this sum is taken as the best model. It reproduces not only the integrated emission well, but also the line shape such that the optical depth of the emission is taken into account properly.

## 4. Results and discussion

### 4.1. Dust temperature and density maps

The final parameters of the hydrogen number density and dust temperature profiles in the cores according to the formulae given in Sect. 3.1 are listed in Table 3. In Figs. B.1–B.7 we show the hydrogen density and dust temperature maps of all globules in the mid-plane across the sky as they were obtained from the continuum data with the ray-tracing technique described in Sect. 3.1. The central density of the starless cores ranges from $4\times10^4$ cm$^{-3}$ to $4\times10^5$ cm$^{-3}$. The cores are clearly non-isothermal, as already predicted by radiative transfer models (e.g., Evans et al. 2001). In all cores the dust temperature drops from the outer rims with 13−19 K to the core centers to 8−13 K. Compared to the temperatures derived from the modified black-body fitting technique in Launhardt et al. (2013), the central temperatures are lower by 1−3 K. The central column densities reach from $7\times10^{21}$ to $6\times10^{22}$ cm$^{-2}$ in the maps derived with the ray tracing technique compared to the column densities of $7.5\times10^{21}$ to $4.6\times10^{22}$ cm$^{-2}$ in Launhardt et al. (2013) which is on average 60% more. The lowest difference is found in the case

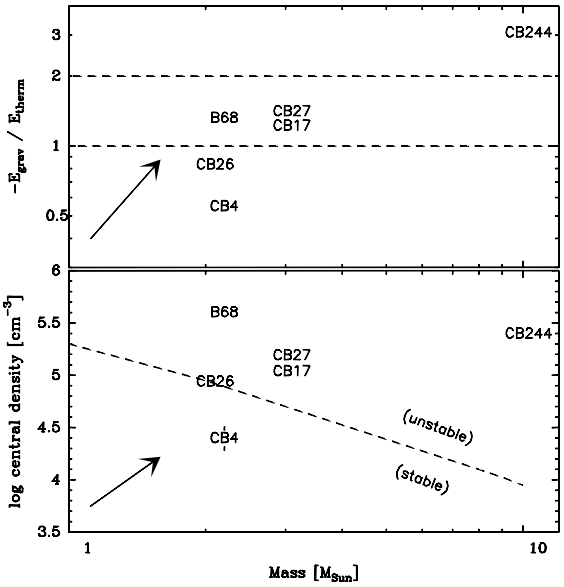


**Fig. 2.** Stability of the cores. Same plot as Fig. 6 in Launhardt et al. (2013), but here for the results of the ray-tracing models. *Top*: ratio of gravitational potential to thermal kinetic energy vs. total gas mass ($M_{core}$). The lower dashed horizontal line marks the bounding limit of $-E_{grav}/E_{therm} = 1$, while the upper line marks the state of virialization at $-E_{grav}/E_{therm} = 2$. *Bottom*: central density vs. total gas mass for the same cores. The dashed line marks the maximum stable density of a pressure-supported, self-gravitating modified (nonisothermal) BES as calculated by Keto & Caselli (2008, with their Fig. 14, model with photoelectric heating at the core boundary taken into account). The uncertainty resulting from the ray-tracing modeling is indicated by the error bars at CB 4. The arrows indicate the maximum systematic shift of the cores in the diagram if grain properties of ISM dust were used in the modeling.

of CB 17 with an increase of only 6% and the highest in the case of B 68 with an increase of 230%.

From the maps we have derived one-dimensional profiles by azimuthally averaging around the centers of the starless cores. The regions that were considered for deriving the radial profiles are indicated with thick white lines in the *SPIRE* 250 $\mu$m maps in Figs. A.1–A.7. Because of its strong asymmetry and the nearby protostellar core, the starless core in CB 130 is not well-suited for a 1D study. We therefore do not derive a radial profile of its density and temperature structure and will also not take it into account for the chemical modeling. The profiles of the hydrogen volume and column density, and dust temperature of the other globules are plotted in Fig. 1.

### 4.2. Sizes, masses, and stability of the cores.

We derived masses of the starless cores by integrating over the circularized 1D hydrogen density profiles $n_H(r)$. We conservatively estimate the mass by choosing $r_1$ (Eq. (2)) as outer radii of the cores where the profiles turn from a power-law like into a flat shape. These radii range from $27 \times 10^3$ to $57 \times 10^3$ AU and are listed in Table 3. We take into account that the total gas mass is higher by a factor of $\mu_H = 1.36$ than the hydrogen atom mass so that the core masses are given by:

$$M_{core} = M(r_1) = \mu_H m_H \times 4\pi \int_0^{r_1} n_H(r) r^2 dr. \quad (5)$$

The resulting core masses range from 2 $M_\odot$ to 10 $M_\odot$ (see Fig. 2) and are well in agreement with those previously estimated from modified black-body fits (see Stutz et al. 2010; Launhardt et al. 2013).

The stability of the cores was checked by comparing the gravitational potential with the thermal energy of the particles in the cores. We neglected turbulent pressure, rotational energy and magnetic fields. This is justified since the thermal energy is the strongest contributor to the stabilization. Assuming typical magnetic field strengths in Bok globules of a few 100 $\mu$G (Wolf et al. 2003), these three contributions are dominated by the turbulent pressure which we have estimated for all cores and typically adds only 10% to the thermal energy.

We estimated the gravitational potential by

$$E_{grav} = -4\pi G m_H \mu_H \int_0^{r_1} M(r) n_H(r) r dr \quad (6)$$

where $G$ is the gravitational constant. The thermal energy of the molecules is calculated from

$$E_{therm} = \frac{3 k_B \mu_H}{2\mu} 4\pi \int_0^{r_1} T(r) n_H(r) r^2 dr \quad (7)$$

where $k_B$ is the Boltzmann constant and $\mu_H n_H/\mu$ with $\mu/\mu_H = 0.6$ the mean particle density for molecular gas. For the gas temperature, we adopt the dust temperature. $T_{Gas}$ might actually be higher than $T_{Dust}$ in the outer regions of the envelopes, so that we probably underestimate $E_{therm}$.

In the top panel of Fig. 2, we plot the ratio of the total gravitational to thermal energy of all starless cores against their masses. The dashed horizontal line at a ratio of 2 indicates virial equilibrium while the dashed line at a ratio of 1 marks the bounding limit. The values for the cores indicate that only the starless core of CB 244 is clearly gravitationally unstable. In Fig. 2 (bottom) we plot the central density against the total mass of the cores. The dashed line indicates the maximum central density of a pressure-supported, self-gravitating modified (non-isothermal) Bonnor-Ebert sphere (BES; Bonnor 1956; Ebert 1955), calculated by Keto & Caselli (2008) for a core with photoelectric heating at the boundary. The comparison of the core properties to the theoretical curve strengthens the result that the starless core in CB 244 is prestellar. It also suggests that CB 17, CB 27, and B 68 are thermally super critical.

### 4.3. Spectra and molecular emission maps

In Figs. A.1–A.7, integrated emission maps of $^{12}$CO ($J = 2{-}1$), $^{13}$CO ($J = 2{-}1$), C$^{18}$O ($J = 2{-}1$) and $N_2H^+$ ($J = 1{-}0$) are presented. For the sake of comparison we also have included maps showing the same regions as observed with the SPIRE bolometer in the 250 $\mu$m band and from the Digitized Sky Survey 2 archive[7]. Because of their different abundances, the emission of three isotopologues becomes optically thick at different column densities. As the main CO isotopologue, $^{12}$CO traces the envelopes of the globules particularly well, while $^{13}$CO is best suited to tracing the outer parts of the cores. As the rarest isotopologue, C$^{18}$O traces the dense regions of the cores up to hydrogen densities of $\sim 1 \times 10^5$ cm$^{-3}$. At these densities CO freezes out onto the dust grains. We therefore complemented our set of molecular line observations with maps of $N_2H^+$, which traces the densest parts of the cores where CO is frozen out. The time scales of build-up and depletion of $N_2H^+$ are longer than for CO so that both species in combination allow constraining the ages of the cores.

[7] http://archive.stsci.edu/cgi-bin/dss_form

**Table 4.** Spectral line parameters at the centers of the starless cores.

| Source | Line | $\Delta v_{\rm chann}$ [m/s] | $v_{\rm LSR}{}^{(a,b)}$ [km s$^{-1}$] | $T_{\rm mb}^{\rm peak\,(a,b)}$ [K] | $\Delta T_{\rm mb}^{\rm RMS}$ [K] | $\Delta v_{\rm FWHM}{}^{(a,b)}$ [km s$^{-1}$] | $\Delta v_{\rm therm}{}^{(c)}$ [km s$^{-1}$] | $\Delta v_{\rm non-therm}$ [km s$^{-1}$] | $I_{\rm line}{}^{(d)}$ [K km s$^{-1}$] |
|---|---|---|---|---|---|---|---|---|---|
| CB 4 | $^{12}$CO(2−1) | 0.325 | −11.423 ± 0.002 | 13.3 ± 0.3 | 0.11 | 0.510 ± 0.007 | 0.15 | 0.49 ± 0.01 | 7.8 ± 0.6 |
| | $^{13}$CO(2−1) | 0.34 | −11.35 ± 0.01 | 7.3 ± 0.6 | 0.22 | 0.45 ± 0.02 | 0.15 | 0.42 ± 0.03 | 4.4 ± 0.3 |
| | C$^{18}$O(2−1) | 0.053 | −11.442 ± 0.004 | 3.5 ± 0.3 | 0.15 | 0.19 ± 0.01 | 0.15 | 0.12 ± 0.04 | 0.73 ± 0.04 |
| | $N_2H^+$(1−0) | 0.063 | −11.355 ± 0.005 | 0.47 ± 0.09 | 0.09 | 0.17 ± 0.02 | 0.15 | 0.08 ± 0.08 | 0.38 ± 0.08 |
| CB 17 | $^{12}$CO(2−1) | 0.325 | −4.74 ± 0.01 | 9.7 ± 0.5 | 0.15 | 0.97 ± 0.03 | 0.14 | 0.96 ± 0.03 | 12.8 ± 0.8 |
| | $^{13}$CO(2−1) | 0.34 | −4.70 ± 0.01 | 6.2 ± 0.4 | 0.19 | 0.71 ± 0.03 | 0.14 | 0.70 ± 0.03 | 2.5 ± 0.4 |
| | C$^{18}$O(2−1) | 0.053 | −4.764 ± 0.004 | 2.4 ± 0.1 | 0.07 | 0.45 ± 0.01 | 0.13 | 0.43 ± 0.02 | 1.2 |
| | $N_2H^+$(1−0) | 0.063 | −4.630 ± 0.001 | 1.5 ± 0.2 | 0.19 | 0.325 ± 0.002 | 0.14 | 0.29 ± 0.01 | 3.0 |
| CB 26 | $^{12}$CO(2−1) | 0.325 | +5.590 ± 0.007 | 3.6 ± 0.1 | 0.08 | 1.17 ± 0.02 | 0.14 | 1.16 ± 0.02 | 6.3 ± 0.3 |
| | $^{13}$CO(2−1) | 0.34 | +5.64 ± 0.01 | 2.7 ± 0.2 | 0.14 | 1.01 ± 0.03 | 0.14 | 1.00 ± 0.03 | 2.3 ± 0.5 |
| | C$^{18}$O(2−1) | 0.053 | +5.60 ± 0.02 | 1.1 ± 0.1 | 0.15 | 0.70 ± 0.04$^{(e)}$ | 0.14 | 0.69 ± 0.04 | 0.73 ± 0.09 |
| | $N_2H^+$(1−0) | 0.063 | $^{(f)}$ | $^{(f)}$ | 0.08 | $^{(f)}$ | $^{(f)}$ | $^{(f)}$ | 0.4 ± 0.1 |
| CB 27 | $^{12}$CO(2−1) | 0.325 | +7.127 ± 0.005 | 4.1 ± 0.1 | 0.08 | 0.89 ± 0.01 | 0.14 | 0.88 ± 0.01 | 4.4 ± 0.2 |
| | $^{13}$CO(2−1) | 0.34 | +7.14 ± 0.02 | 3.4 ± 0.05 | 0.10 | 0.61 ± 0.05 | 0.14 | 0.59 ± 0.06 | 2.2 ± 0.3 |
| | C$^{18}$O(2−1) | 0.053 | +7.058 ± 0.005 | 3.0 ± 0.2 | 0.16 | 0.24 ± 0.01 | 0.13 | 0.20 ± 0.02 | 0.78 ± 0.06 |
| | $N_2H^+$(1−0) | 0.063 | +7.104 ± 0.001 | 2.1 ± 0.08 | 0.08 | 0.187 ± 0.004 | 0.14 | 0.12 ± 0.03 | 2.15 ± 0.07 |
| B 68 | $^{12}$CO(2−1) | 0.325 | +3.30 ± 0.01 | 5.9 ± 0.4 | 0.16 | 0.63 ± 0.02 | 0.14 | 0.61 ± 0.03 | 4.4 ± 0.3 |
| | $^{13}$CO(2−1) | 0.34 | +3.35 ± 0.01 | 3.1 ± 0.5 | 0.12 | 0.51 ± 0.05 | 0.14 | 0.49 ± 0.06 | 1.8 ± 0.3 |
| | C$^{18}$O(2−1) | 0.030 | +3.292 ± 0.001 | 2.10 ± 0.02 | 0.02 | 0.200 ± 0.001 | 0.14 | 0.14 ± 0.02 | 0.45 ± 0.04 |
| | $N_2H^+$(1−0) | 0.063 | +3.347 ± 0.001 | 0.88 ± 0.01 | 0.01 | 0.249 ± 0.003 | 0.14 | 0.21 ± 0.02 | 1.5 ± 0.04 |
| CB 130 | $^{12}$CO(2−1) | 0.051 | $^{(g)}$ | 2.3$^{(h)}$ | 0.08 | 4.2$^{(i)}$ | 0.14 | .. | 11.6 ± 0.1 |
| | $^{13}$CO(2−1) | 0.053 | +7.60 ± 0.01 | 1.2 ± 0.1 | 0.07 | 1.26 ± 0.04$^{(e)}$ | 0.14 | 1.25 ± 0.04 | 1.8 ± 0.1 |
| | C$^{18}$O(2−1) | 0.053 | +7.524 ± 0.006 | 0.96 ± 0.05 | 0.05 | 0.48 ± 0.01 | 0.14 | 0.46 ± 0.02 | 0.52 ± 0.03 |
| | $N_2H^+$(1−0) | 0.063 | +7.514 ± 0.002 | 1.34 ± 0.04 | 0.04 | 0.397 ± 0.005 | 0.14 | 0.37 ± 0.01 | 3.2 ± 0.05 |
| CB 244 | $^{12}$CO(2−1) | 0.325 | +3.407 ± 0.008 | 4.2 ± 0.1 | 0.05 | 1.62 ± 0.02 | 0.13 | 1.61 ± 0.02 | 7.5 ± 0.5 |
| | $^{13}$CO(2−1) | 0.34 | +3.86 ± 0.01 | 2.5 ± 0.1 | 0.07 | 0.98 ± 0.03 | 0.13 | 0.97 ± 0.03 | 2.7 ± 0.2 |
| | C$^{18}$O(2−1) | 0.053 | +3.805 ± 0.007 | 3.0 ± 0.2 | 0.19 | 0.43 ± 0.02 | 0.13 | 0.41 ± 0.03 | 1.2 ± 0.1 |
| | $N_2H^+$(1−0) | 0.063 | +3.875 ± 0.002 | 1.90 ± 0.08 | 0.08 | 0.34 ± 0.005 | 0.13 | 0.31 ± 0.01 | 4.6 ± 0.2 |

**Notes.** $^{(a)}$ For the CO isotopologues determined from Gaussian fits, for $N_2H^+$ determined from fits of the hyperfine structure, $^{(b)}$ for $N_2H^+$ of the main line at 93 173.777 MHz, $^{(c)}$ assuming a constant gas temperature along the LoS that is equal to the dust temperature derived from modified black body fitting. We estimate an uncertainty of 0.02 km s$^{-1}$. $^{(d)}$ Determined by integrating of the spectra (in the case of $N_2H^+$ all components). $^{(e)}$ This line is double peaked. The linewidth given here is given for a Gaussian fitted to the full spectrum, $^{(f)}$ not detected, $^{(g)}$ not determinable, $^{(h)}$ not fit with a Gaussian. Peak value taken directly from the spectrum., $^{(i)}$ not fit with a Gaussian. Width of spectrum where $T_{\rm mb} > 0.5 T_{\rm mb}^{\rm peak}$.

The $^{12}$CO and $^{13}$CO maps are smaller than the *SPIRE* 250 $\mu$m maps, but the molecular emission of $^{12}$CO is more extended than the continuum emission in some cases. This indicates that there are extended cold envelopes to which the continuum observations are less sensitive. C$^{18}$O is the least abundant CO isotopologue used in this study. It is therefore the optically thinnest and best suited CO isotopologue for the dense regions of the cores where CO is not frozen out. While its emission is enhanced at the positions of some Class I objects, it does not show enhancement at the locations of the starless cores. In contrast, the $N_2H^+$ emission shows a positive gradient towards the core centers. In the two least dense starless cores, CB 4 and CB 26, $N_2H^+$ emission was only marginally detected.

The spectral line parameters at the centers of the starless cores are listed in Table 4. The spectra of all molecules toward the centers of the starless cores are also plotted in Fig. 3. C$^{18}$O is single-peaked in all sources except CB 26, where two distinct peaks at a velocity separation of 0.33 km s$^{-1}$ are observed. It is unlikely that the dip is due to self-absorption, since the line is quite weak. It is more likely caused by multiple velocity components. Almost no $N_2H^+$ emission is detected from the starless core in CB 26. At the position of the protostar in CB 26, the C$^{18}$O line is also double peaked, with the dip at the same velocity as for the starless core. This is an indication of the protoplanetary disk seen edge-on (Launhardt & Sargent 2001). The peak main beam temperature $T_{\rm MB}$ of the C$^{18}$O ($J$ = 1−0) transition ranges from 2 K to 6 K in the various globules.

The channel width of the $^{13}$CO observations is only 0.34 km s$^{-1}$ compared to 0.05 km s$^{-1}$ of the C$^{18}$O spectra. If the $^{13}$CO line of CB 26 was double peaked as the C$^{18}$O line, we could not resolve it. The $^{13}$CO line is single peaked in all cores except for CB 130 where it shows two peaks with a velocity separation of 0.53 km s$^{-1}$. The dip of this line falls into the peak of the C$^{18}$O emission and is thus probably a result of self-absorption.

The emission of the main isotopologue $^{12}$CO is optically thick towards the core centers but traces also the outskirts of the globules where the emission of the less abundant isotopes drops below the detection limit. Consequently, its linewidth is highest throughout the sample and ranges from 0.3 km s$^{-1}$ to 0.7 km s$^{-1}$ in the globules that only contain starless cores. In those globules that also inhabit protostellar cores, the linewidths are generally higher and reach values of up to 1.6 km s$^{-1}$. CB 130 is an exceptional case with a very broad line emission, consistent with its location within a larger diffuse structure.

All globules show signs of slow large-scale motions. The linewidths are typically larger than the thermal linewidths and increase from the rare to the abundant CO isotopologues. The

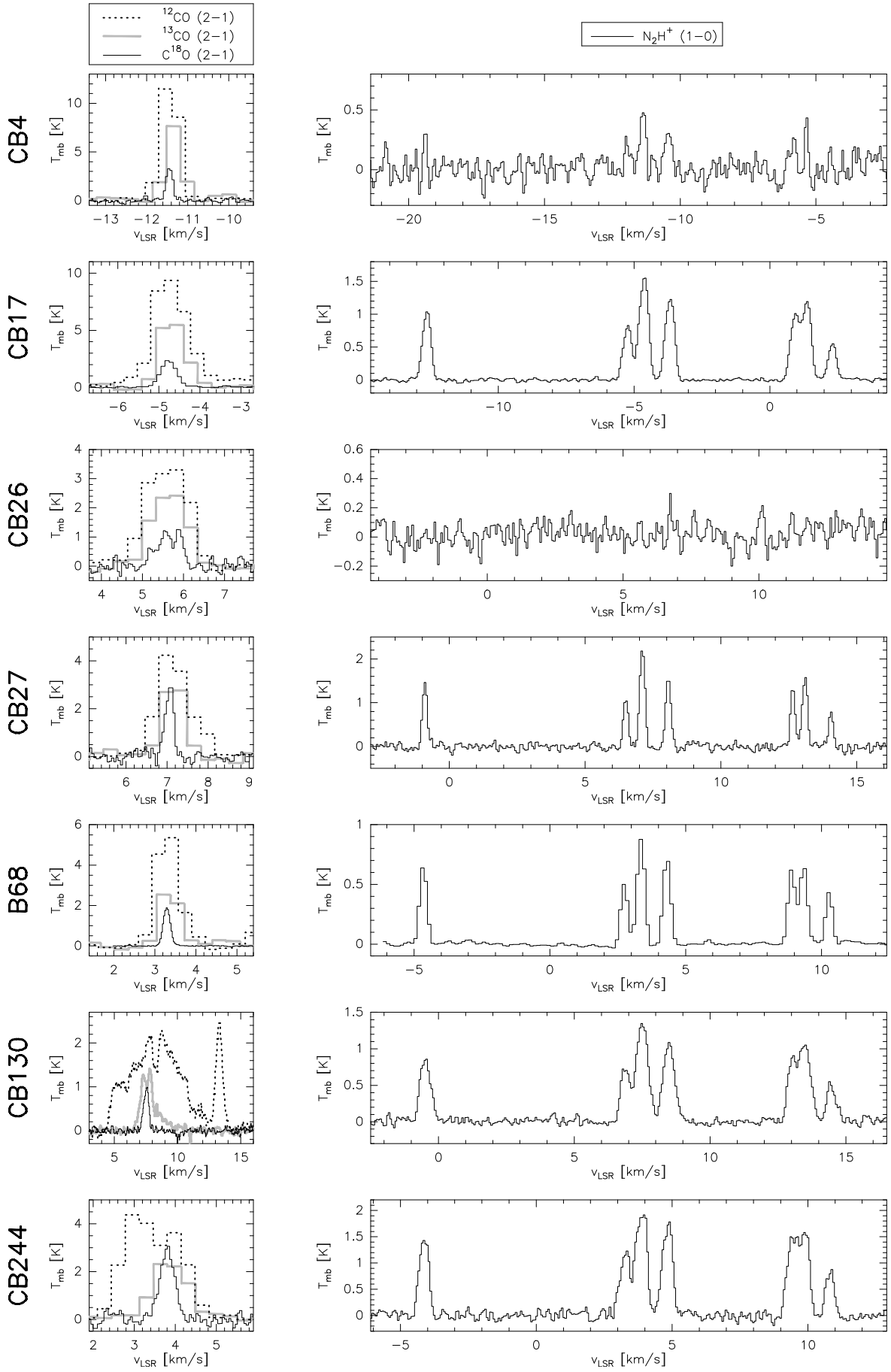


**Fig. 3.** Spectra of the $^{12}$CO (2–1), $^{13}$CO (2–1), C$^{18}$O (2–1) and $N_2H^+$ (1–0) transitions in a 36.4″ HPB at the centers of the starless cores.

average linewidths of the spectra toward the core centers are 0.30 km s$^{-1}$, 0.69 km s$^{-1}$, and 1.0 km s$^{-1}$ for C$^{18}$O, $^{13}$CO, and $^{12}$CO, respectively. The thermal linewidths are typically around 0.15 km s$^{-1}$, if one assumes that the gas temperature is equal to the dust temperature. The radiation of $^{13}$CO and $^{12}$CO emanate mainly from regions with $n_{\rm H} \lesssim 10^4$ cm$^{-3}$ where the gas is expected to be warmer than the dust, since the density is too low to couple both temperatures via collisions. Therefore, a fraction of the linewidth increase can be attributed to higher gas temperatures at the outskirts of the globules. Gas temperatures of 30 K to 50 K would, however, only result in a thermal line broadening of 0.22 km s$^{-1}$ to 0.29 km s$^{-1}$, respectively. The remaining broadening must be caused by turbulent or macroscopic motions, but is partly also mimicked by the optical thickness of the lines.

With the $N_2H^+$ observations we trace the inner part ($r \lesssim 10^4$ AU) of the cores where large amounts of CO are expected to be frozen out onto the dust grains. The spectra at the position of the core centers are shown in Fig. 3 (right panels). The linewidths range from 0.08 km s$^{-1}$ up to 0.37 km s$^{-1}$. This range can only partially result from different temperatures and must have its origin in the different dynamics of the gas.

### 4.4. Core properties constrained from chemical modeling

On the basis of the dust temperature and hydrogen density profiles presented in Sect. 4.1, we have modeled the chemical evolution of the globules. The approach is explained in Sect. 3.2. The best fits of the modeled integrated emission to the observed profiles are presented in Fig. 4. In Fig. 5, we demonstrate the quality of the agreement between modeled and observed line shapes.

#### 4.4.1. The individual globules

*CB 4:* while CB 4 is the most symmetric and isolated globule of our study (Fig. A.1), it is also the least dense one with a central hydrogen density of only $4 \times 10^4$ cm$^{-3}$. It is the only core in the study for which the modeled $^{13}$CO emission is underestimated with all parameter sets. Owing to its low density, the coupling of gas and dust temperature is expected to be the weakest in this globule and the gas temperature might thus be significantly higher than the dust temperature. The emission of C$^{18}$O and $N_2H^+$ is dominated by inner regions such that the gas temperature is closer to the dust temperature. We find that the chemical age of CB 4 is $\sim 10^5$ yr. The significance of the derived chemical ages is discussed in Sect. 4.4.4. To match the observations, we have to increase the hydrogen density by a factor of 3. We require $A_{V,\,\rm out}$ to be set at a value of at least 4 mag, while a value of 0.6 mag has been derived from the NIR extinction maps.

*CB 17:* the $^{13}$CO emission of CB 17 can be reproduced assuming a chemical age of $7 \times 10^4$–$10^5$ yr and assuming that the hydrogen density is increased by a factor of 3. We only have a very small map of C$^{18}$O emission for this source, such that the observational constraint to the model is limited. We find the best fit for an age of $5 \times 10^4$–$10^5$ yr. The best model for $N_2H^+$ is found at a chemical age of $10^5$ yr. We find the best fits for an external visual extinction of 2 mag that is also found from the NIR extinction mapping, but the deviation is not strong for $A_{V,\,\rm out}$ values ranging from 0 to 6 mag. Our finding of a low chemical age does not confirm the finding of Pavlyuchenkov et al. (2006) who found a chemical age of 2 Myr for the starless core in CB 17.

*CB 26:* we reproduce the $^{13}$CO emission from the starless core in CB 26 with a chemical age of $4 \times 10^5$ yr. The emission profile of C$^{18}$O, however, is very steep and shows no signatures of freezeout. It is best described with chemical models at an age of only $\sim 10^4$ yr and by setting the external visual extinction at the model boundary to 0 ($A_{V,\,\rm out} = 1$ in the NIR extinction map). The parameters are consistent with the very weak observed emission of $N_2H^+$.

*CB 27:* the $^{13}$CO emission of CB 27 cannot be fit well. In particular, the emission coming from large radii is underestimated in all our models. This discrepancy can be overcome if an increased gas temperature in the envelope of this core is assumed. The range of chemical ages, for which the models fit the data similarly well within the uncertainties, is wide and reaches from $10^5$ to $10^6$ yr. For the C$^{18}$O emission, we find the best models at $A_{V,\,\rm out}$ values ranging from 2 to 6 mag ($A_{V,\,\rm out} = 1$ has been found in the NIR-extinction map) and an age between $5 \times 10^4$ and $10^5$ yr. The hydrogen density needs to be multiplied by a factor of 3 with respect to the density profiles obtained from the EPoS project. The $N_2H^+$ emission is modeled best with the same age as the C$^{18}$O emission but only a factor 2 in density.

*B 68:* this is the only core for which all three molecular emission profiles can be reproduced from our chemical models with the hydrogen density profile as derived in Sect. 4.1. If we increase the hydrogen density in the models, the resulting molecular emission profiles deviate significantly from the observed profiles. The best chemical age to match the $^{13}$CO observations is $2 \times 10^5$ yr, while we find that the C$^{18}$O and $N_2H^+$ profiles are best explained by models with a chemical age between $7 \times 10^4$ and $10^5$ yr. Bergin et al. (2006) found an chemical age of $\sim 10^5$ yr from chemical modeling and a comparison of the modeled and observed $^{13}$CO and C$^{18}$O emission. This is well in agreement with our findings, and $A_{V,\,\rm out}$ needs to be around 4–6 mag in the models while we derived a value of about 1 mag from the NIR extinction map.

*CB 244:* as for CB 27, all our models underestimate the $^{13}$CO emission at large radii, which could be explained by a decoupling of dust and gas temperatures at low densities. The chemical age that fits the data best is around $2 \times 10^5$ yr. In contrast, the C$^{18}$O and $N_2H^+$ profiles are best fit with a chemical age of only $4 \times 10^4$ yr. Changing the external $A_v$ at the model boundaries does not have a significant impact on the goodness of the fits. The hydrogen density needs to be multiplied by 2 for the CO isotopologues and by a factor of 3 for $N_2H^+$.

That we obtain a discrepancy of a factor $\sim$2–3 is an indication that the assumed dust model may be incorrect. This result is discussed in Sect. 4.4.6.

#### 4.4.2. CO abundances

In Fig. 6, we plot the modeled relative abundance profiles of gaseous and frozen C$^{18}$O of the final models that correspond to the emission profiles presented in Fig. 4. The abundance of gaseous C$^{18}$O ($X(\mathrm{C^{18}O}) \equiv n(\mathrm{C^{18}O})/n_{\rm H}$) in molecular gas that is assumed to be shielded well and undepleted varies in the literature and ranges from $3.5 \times 10^{-8}$ (Tafalla & Santiago 2004) to $2.4 \times 10^{-7}$ (Lee et al. 2003). In the outer parts of all our cores, the C$^{18}$O abundances $X$(C$^{18}$O) reach the value of Tafalla & Santiago (2004). The highest abundance of $9 \times 10^{-8}$ is reached in the envelope of the young and not that dense core CB 26. The hydrogen densities in the regions of maximum C$^{18}$O abundances are typically between $10^4$ and $5{\times}10^4$ cm$^{-3}$. In the center of the cores, the gaseous C$^{18}$O abundance drops because of freezeout onto the dust grains. There, the C$^{18}$O abundance (relative to the peak abundance) drops by a factor of 2 in the least dense core (CB 4) and by a factor of 30 in the denser cores (CB 27, B 68, and CB 244). Towards the outer edges, CO is photodissociated by

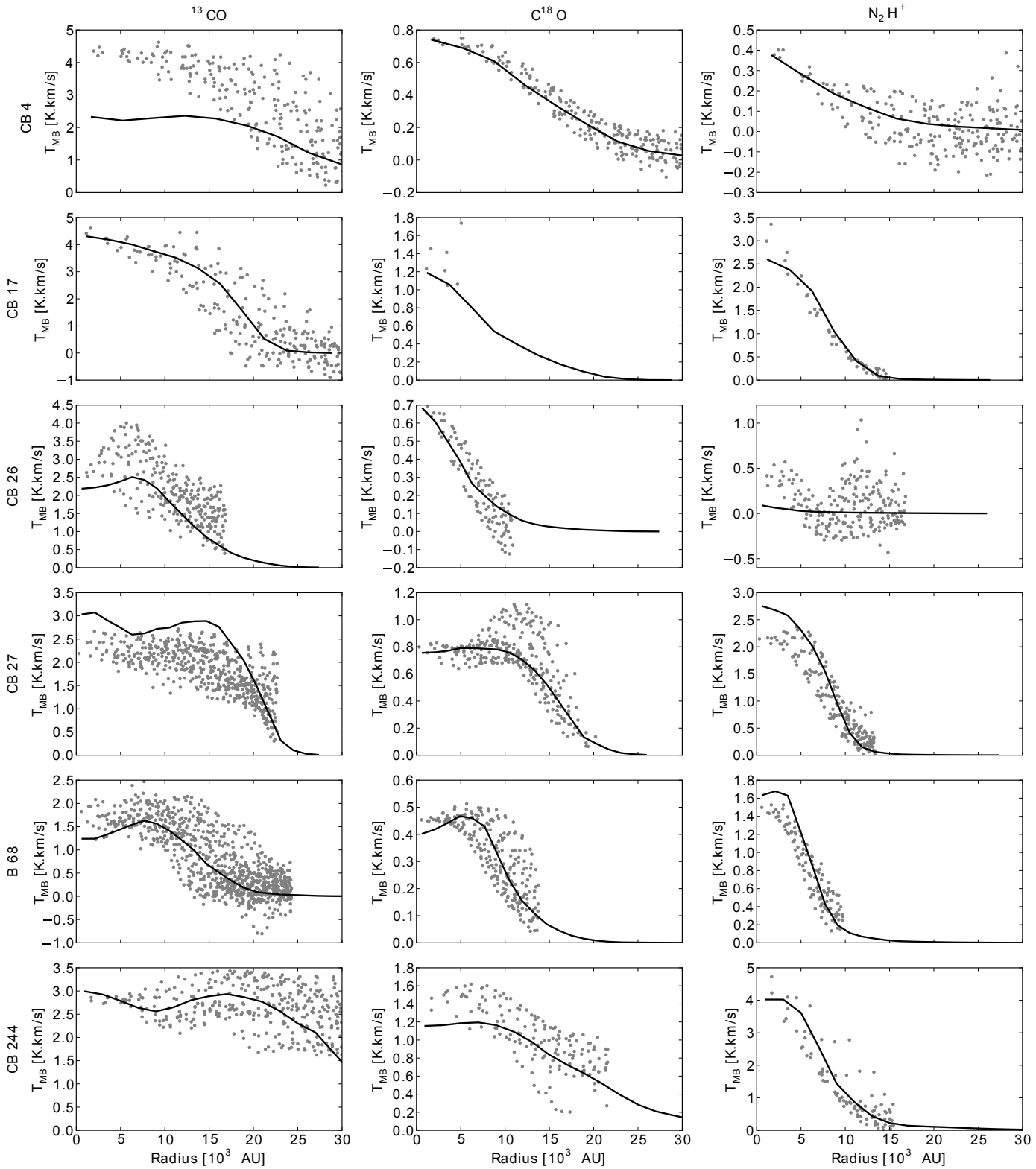


**Fig. 4.** Profiles of the integrated emission that would result from the molecular abundances of the final models (solid line) compared to the observed profiles of the integrated emission for all modeled starless cores. (*Left*) $^{13}$CO ($J$ = 2–1), (*center*) C$^{18}$O ($J$ = 2–1), (*right*) $N_2H^+$ ($J$ = 1–0).

UV radiation, so that $X(C^{18}O)$ there also drops. The emission profiles of $^{13}$CO are not reproduced as well by the chemical models as for C$^{18}$O (see Fig. 4). The reason for this is most likely that the emission of this molecule is dominated from the outer envelope, which is probably warmer than the dust in the same layers. Thus, the observed emission profiles are flatter and extended further towards larger radii than is the case in the models. The optical thickness of the lines becomes apparent, for, instance, in the modeled emission profile of CB 244 (Fig. 4). The density distribution of this model peaks at a radius of about $2 \times 10^4$ AU.

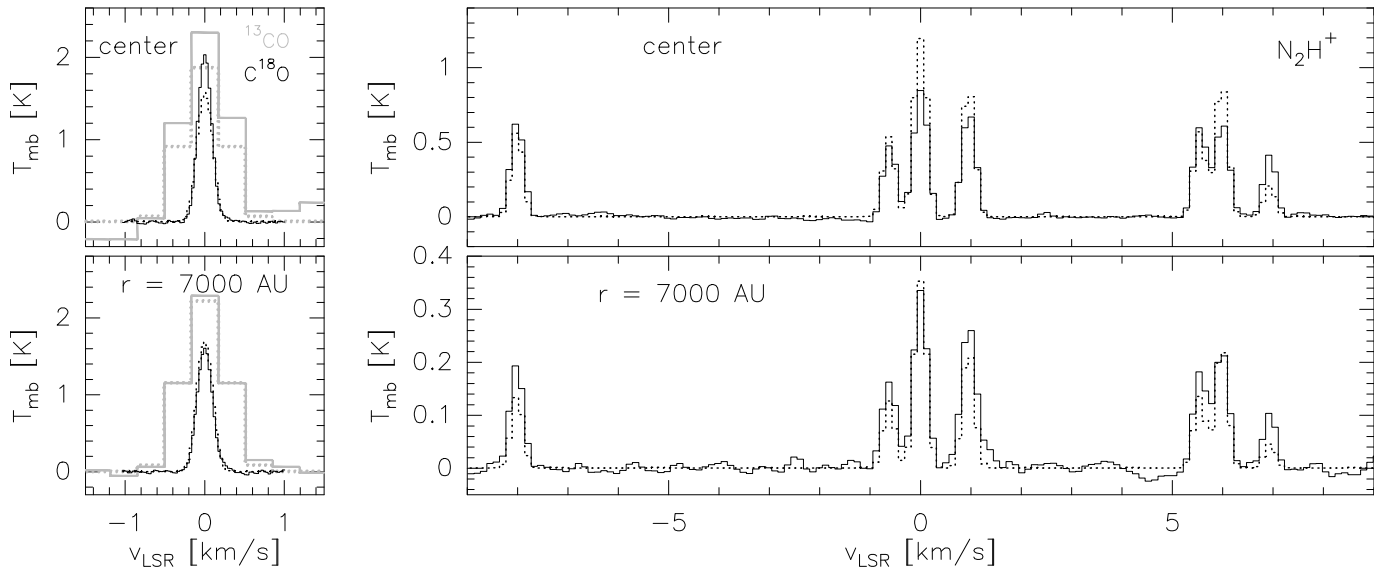


**Fig. 5.** To quantify the agreement of models and observations we compare the spectra over the full radius of the models. Here, an example of B 68 is shown. The solid lines represent observations, the dotted lines the synthetic spectra of the best models. On the *left panels*, we show the spectra of the $^{13}$CO ($J$ = 2–1) (gray) and C$^{18}$O ($J$ = 2–1) (black) transitions. On the *right panels*, we show the spectra of the $N_2H^+$ ($J$ = 1–0) transition. The top line shows the spectra at the position of the core center, the bottom line the spectra at a radial distance of 7000 AU.

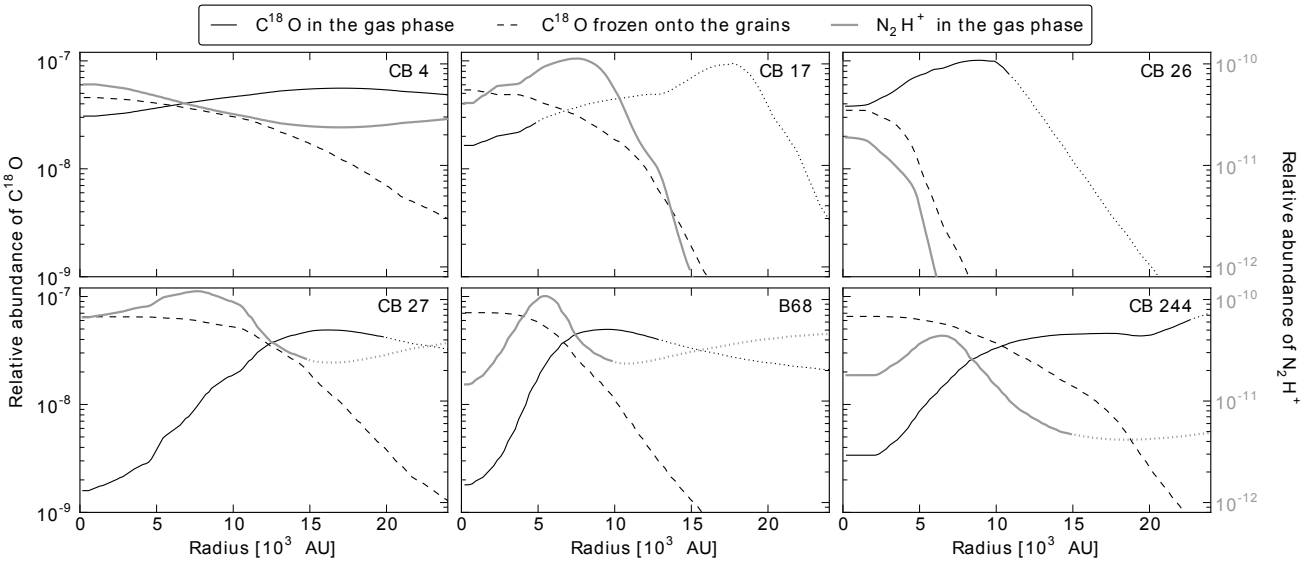


**Fig. 6.** Relative abundances (absolute molecular density with respect to the hydrogen density) of gaseous C$^{18}$O (black solid line), frozen-out C$^{18}$O (dashed black line) and gaseous $N_2H^+$ (gray solid line) in the final models. At the outer radii of the emission profiles derived from the observations, the lines turn from a solid into a dotted line shape, indicating that these parts of the profiles are not constrained by observations.

The drop towards smaller radii is still indicated in the emission profile, but towards even smaller radii, it is dominated by the warm outer layer so that it even rises, thus explaining the double-peaked $^{13}$CO emission profiles in CB 27 and CB 244 (Fig. 4).

We also plot the profiles of icy C$^{18}$O since they are predicted by the best-fit chemical models in Fig. 6. Its amount in the core center is in some cases greater than the amount of gaseous C$^{18}$O at its peak position, since at high densities the CO production is faster than the freezeout of atomic C. If the abundances of icy C$^{18}$O at the core centers are compared to the total C$^{18}$O abundance there, the ratios range from 45% in CB 4 to more than 90% in those cores that have a central hydrogen density of more than $10^5$ cm$^{-3}$. In Fig. 7, we compare these ratios in all cores and correlate them to the core radius, the hydrogen volume and column densities, and the dust temperature. The freezeout increases towards the core centers and with increasing hydrogen densities. The total temperature range between $T_{in}$ and $T_{out}$ in the cores is less than 10 K, and the correlation of freezeout with the temperature is not as clear as for the other quantities. Typically, half of the total C$^{18}$O molecules stick to the grains at a radius of ~$10^4$ AU, a hydrogen density of ~$10^5$ cm$^{-3}$, and a temperature of 11 K. In Table 5 we list the maximum level of freezeout in the individual cores and the conditions at which half of the total C$^{18}$O molecules are frozen onto the dust grains. The correlation of the freezeout level to the hydrogen densities is plotted for the conditions of the core centers in Fig. 8.

#### 4.4.3. $N_2H^+$ abundances

$N_2H^+$ forms and depletes on longer time scales than CO. We find that in four out of the six studied globules (those with a central density over $10^5$ cm$^{-3}$), $N_2H^+$ is strongly depleted in the core

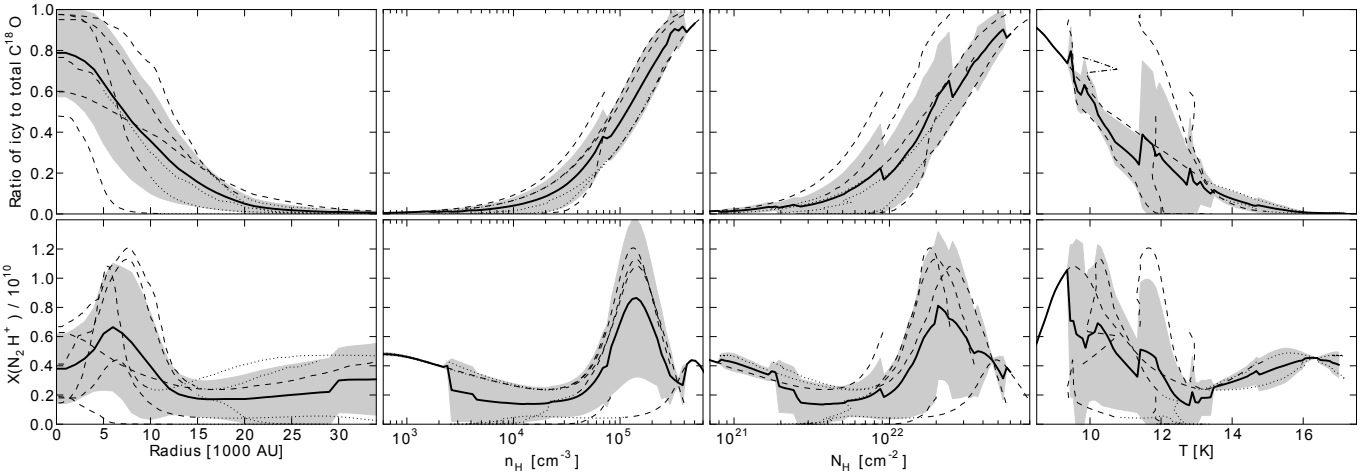


**Fig. 7.** *Top row*: the ratio of icy-to-total $C^{18}O$ abundance of the best-fit models is plotted against the core radius, the hydrogen number density, the column density, and the dust temperature. *Bottom row*: the $N_2H^+$ abundance (relative to the hydrogen density) is plotted against the same quantities. The dashed lines indicate the results of the individual globules. Where the models cannot be compared to observations (because the line radiation is too weak), the dashed lines turn into dotted lines. The bold solid lines mark the mean values. The gray area indicates one standard deviation.

**Table 5.** Ratio of icy to total $C^{18}O$ abundance abundance in the core centers, radius, hydrogen column density, hydrogen density, and dust temperature at which 50% of the total $C^{18}O$ abundance is frozen onto the grains.

| | $X(sC^{18}O)/X(C^{18}O)$ [%] | $R(50\%)$ [AU] | $N_H(50\%)$ [$cm^{-2}$] | $n_H(50\%)$ [$cm^{-3}$] | $T_D(50\%)$ [K] |
|---|---|---|---|---|---|
| CB 4 | 60 | 6000 | $7.7 \times 10^{21}$ | $5.7 \times 10^4$ | 12.9 |
| CB 17 | 77 | 9000 | $1.6 \times 10^{22}$ | $1.5 \times 10^5$ | 11.1 |
| CB 26 | 48 | ... | ... | ... | ... |
| CB 27 | 98 | 12 000 | $1.1 \times 10^{22}$ | $8.2 \times 10^4$ | 12.5 |
| B 68 | 98 | 7000 | $1.8 \times 10^{22}$ | $8.9 \times 10^4$ | 10.5 |
| CB 244 | 95 | 10 000 | $2.8 \times 10^{22}$ | $1.6 \times 10^5$ | 9.8 |

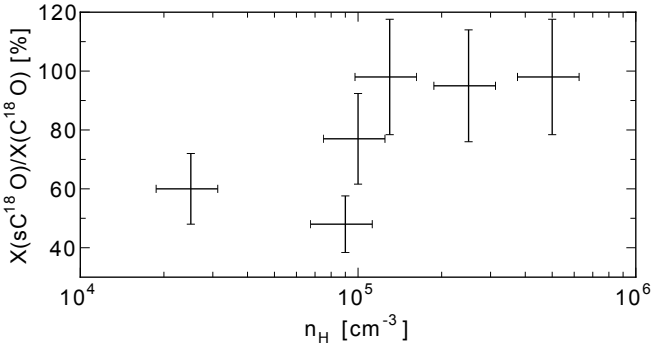


**Fig. 8.** Correlation of $C^{18}O$ freezeout and hydrogen density in the core centers. The horizontal error bars on the hydrogen density represent the fitting uncertainty of the ray-tracing modeling (i.e., excluding systematic uncertainties from, e.g., the dust opacity model; see Sect. 3.1). The vertical error bars represent a 20% uncertainty in the amount of icy CO in the chemical model.

**Table 6.** Ratio of the $N_2H^+$ abundance in the core centers to the maximum abundance, corresponding radius, hydrogen density, and dust temperature.

| | Ratio [%] | $R_{max}$ [AU] | $n_{H,max}$ [$cm^{-3}$] | $T_{D,max}$ [K] |
|---|---|---|---|---|
| CB 17 | 36 | 7500 | $4.7 \times 10^4$ | 10.2 |
| CB 27 | 55 | 7700 | $6.5 \times 10^4$ | 11.7 |
| B 68 | 13 | 5400 | $1.4 \times 10^5$ | 9.5 |
| CB 244 | 41 | 6400 | $1.6 \times 10^5$ | 9.5 |

centers. For comparison, we show in Appendix C that a simple LoS, averaged LTE-analysis would not reveal depletion of $N_2H^+$, although the emission is optically thin ($\tau \lesssim 0.5$) in all cores as we have derived for calculating the molecular column densities in Appendix C. The ratios of the central to maximum abundance of $N_2H^+$ molecules are listed in Table 6. They range from 13% to 55%. The radii, hydrogen density, and dust temperature at which the $N_2H^+$ abundances reach their maximum are also given in Table 6. CB 4 and CB 26 do not show detectable depletion of $N_2H^+$. CB 4 is probably not dense enough and CB 26 might be too young to show depletion at its low central density (see Sect. 4.4.4). The correlation of $X(N_2H^+)$ with core radii, hydrogen volume, and column density and with temperature are plotted for all cores in the bottom row of Fig. 7. $X(N_2H^+)$ typically peaks at hydrogen densities of $10^5$ $cm^{-3}$ in cores at a chemical age of $10^5$ yr. The mean radius of the peak $X(N_2H^+)$ is $(6800 \pm 1000)$ AU. We resolve the regions of $N_2H^+$ depletion in all cores, since these radii are two to three times larger than the half beamwidth.

We find that the depletion of $N_2H^+$ is more restricted to the center as compared to the depletion of CO. It occurs at hydrogen densities $\gtrsim 10^5$ $cm^{-3}$ and column densities $>10^{22}$ $cm^{-2}$, and requires a chemical age of $\gtrsim 10^5$ yr. This finding is consistent with the work of Bergin et al. (2002) on B 68, while other studies have claimed that depletion of N-bearing species

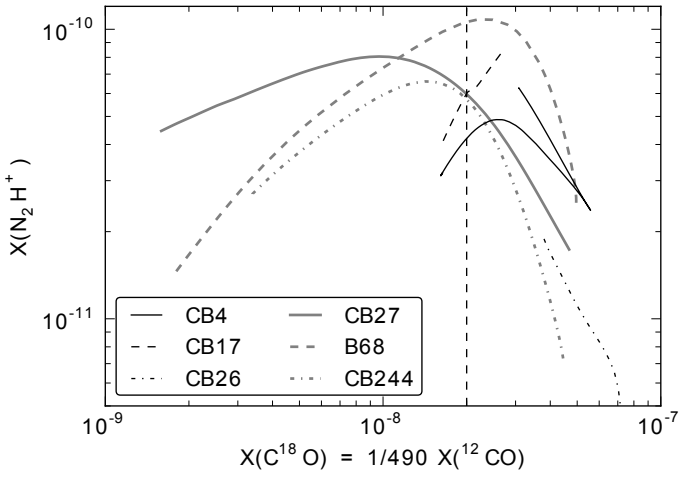


**Fig. 9.** Relative gas phase abundance of $C^{18}O$ against that of $N_2H^+$. At $X(C^{18}O) \approx 2\times10^{-8}$ the correlations turn into an anti-correlation. While at high $X(C^{18}O)$, the $N_2H^+$ molecules are destroyed by reactions with CO, at low $X(C^{18}O)$ (and high densities) freezeout of nitrogen is the dominant reason for depletion of $N_2H^+$.

**Table 7.** Chemical ages of the best fit models for $^{13}CO$, $C^{18}O$, and $N_2H^+$.

| | Chem. age of $^{13}CO$ [yr] | Chem. age of $C^{18}O$ [yr] | Chem. age of $N_2H^+$ [yr] |
|---|---|---|---|
| CB 4 | ... | $10^5$ | $10^5$ |
| CB 17 | $7\times10^4$ | $4\times10^4$ | $10^5$ |
| CB 26 | $4\times10^5$ | $10^4$ | $7\times10^4$ |
| CB 27 | $2\times10^5$ | $7\times10^4$ | $10^5$ |
| B 68 | $2\times10^5$ | $7\times10^4$ | $10^5$ |
| CB 244 | $2\times10^5$ | $4\times10^4$ | $4\times10^4$ |

would only occur at hydrogen densities $\gtrsim10^6$ cm$^{-3}$ (Tafalla et al. 2002; Pagani et al. 2005). The abundance quickly increases outwards and peaks where the majority of CO is still frozen onto the grains. Farther out, it drops where CO becomes abundant in the gas phase. In Fig. 9, we plot the relative gas phase $C^{18}O$ abundance against that of $N_2H^+$ for all globules. The $N_2H^+$ and $C^{18}O$ abundances are anticorrelated at $C^{18}O$ abundances above $10^{-8}$ (corresponding to $X(CO) = 5\times10^{-6}$ when assuming $X(CO)/X(C^{18}O) = 490$), but the curves turn over to a positive gradient below this value. At this point, depletion of nitrogen mainly in form of N and $N_2$ becomes the dominant reason for depletion of $N_2H^+$ compared to reactions with CO.

#### 4.4.4. Chemical age of the cores

"Chemical age" is a parameter in the modeling process. It sets the time span during which the gas develops starting from a state of purely atomic gas of 13 different elements. In this period complex molecules build up and deplete onto the grains. We find that the individual species are fitted best for models of different chemical ages. They are listed in Table 7. The average chemical age of the $^{13}CO$ best-fit models is $(2\pm1)\times10^5$ yr, for $C^{18}O$ $(6\pm3)\times10^4$ yr, and for $N_2H^+$ $(9\pm2)\times10^4$ yr. Up to an age of $\sim2\times10^5$ yr, the chemical models evolve quickly so that deviations of a few $10^4$ yr already lead to significantly worse fits of the models to the data. Therefore, the difference in the chemical ages of the best-fit models between the individual species is significant. $^{13}CO$ that mainly traces the outer envelope of the cores is modeled best with chemical ages that are on average more than $10^5$ yr higher than those of the best-fit models of $C^{18}O$ and $N_2H^+$.

We interpret this finding as the result of core contraction and cooling during the chemical evolution. This would accelerate the freezeout of CO and the synthesis of $N_2H^+$ molecules. Since we assume a constant physical structure in the chemical modeling, we would thus systematically underestimate the chemical age of those species that trace the regions that have been contracting during the chemical evolution. Additional support for this hypothesis is provided by the analysis of the gravitational stability of the cores in Sect. 4.2. We found there that four cores are thermally supercritical and might be gravitationally unstable. This finding is less profound for the other two cores, but cannot be excluded.

Other effects that are not included in our model, such as nonthermal desorption processes like explosive desorption (Shalabiea & Greenberg 1994) or exothermic reactions in the grain mantles (Garrod et al. 2007), might also lead to underestimating the chemical ages. Also, turbulent diffusion (Xie et al. 1995; Willacy et al. 2002) of the gas and grains within the cores can decelerate the chemical aging. Coagulation of the dust grains in the dense part would also slow down the chemical evolution, since by this the grain surface area and thus the rate of grain surface reactions are reduced. In Sect. 4.4.6 we show, however, that the bulk of the dust in these globules cannot be significantly processed and coagulated. Accounting for these combined intrinsic uncertainties in the density structures of the cores, uncertainties associated with chemical reaction rates, and a range of grain sizes in the depletion zone of the cloud, we estimate that the best-fit chemical ages are between $10^5$ and $10^6$ years. This is consistent with a prestellar core lifetime of 0.3–1.6 Myr as derived by Lee & Myers (1999).

#### 4.4.5. Strength of the impacting UV-field

Changing the parameter $A_{v,\mathrm{out}}$ that accounts for the unconstrained extent of the dusty material around the globules in the chemical models has effects that cannot always be clearly distinguished from changing either the hydrogen density or the gas temperature. Nevertheless, the observations are modeled better if $A_{v,\mathrm{out}}$ is increased for half of the globules by a few mag relative to the values that have been measured with NIR extinction mapping (which range from 0.2 to 2 mag for the different globules at the model boundaries). This is probably not a result of overestimating the ISRF in the chemical models. Launhardt et al. (2013) derived the total FIR/mm luminosity of the globules, and it is approximately equal for all of them to the luminosity of the "standard UV-field" (Draine 1978) impacting on spheres of the size of the globules. The same field is also adopted in the chemical modeling, so we do not overestimate its strength.

In the envelopes of the globules at hydrogen densities below $10^4$ cm$^{-3}$, gas and dust temperatures are expected to be decoupled. Since we assume equal gas and dust temperatures in the modeling, we introduce systematic errors in our analysis. In particular, the emission of the gas in the envelopes is underestimated. With a large $A_{v,\mathrm{out}}$ we artificially compensate for this error. The additional shielding protects the molecules from being photodissociated and thus increases their abundance. This hypothesis is supported when comparing $A_{v,\mathrm{out}}$ of the best models to $A_{v,\mathrm{NIR}}$, which are the values derived from the NIR extinction maps. Both values appear to be anticorrelated, and while we do not need to increase $A_{v,\mathrm{out}}$ with respect to the observed values

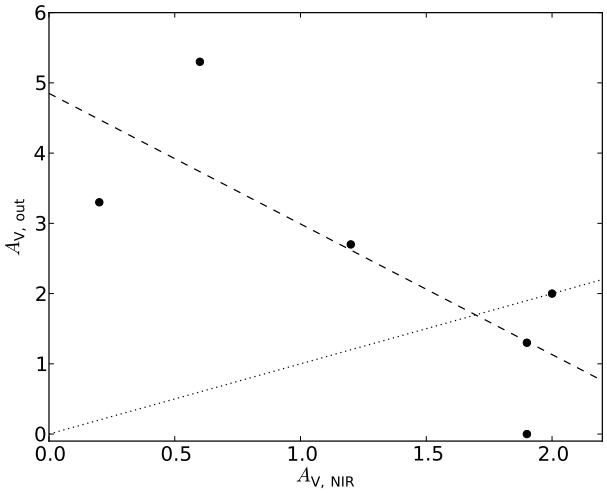


**Fig. 10.** We plot the parameters $A_{v,\,out}$ of the best models over the measured values of $A_{v,\,NIR}$ from the NIR extinction maps. The dashed line is a linear fit to the data points, which is only meant to illustrate the trend. The dotted line indicates $A_{v,\,out} = A_{v,\,NIR}$. We interpret the anti-correlation as an indication of increasing decoupling of gas and dust temperatures towards lower extinction.

at $A_{v,\,NIR} \sim 2$ mag, we have to increase it by more than 3 mag for the least shielded cores. Because of these uncertainties, we think that the need to increase $A_{v,\,out}$ is not convincing evidence that the globules are in fact shielded more strongly from UV-radiation than inferred from NIR-extinction maps.

A direct measurement of the gas temperature in the envelopes would of course be desirable as a constraint for the chemical modeling. Furthermore, in comparison to the dust temperature it would allow distinguishing between shielding from extended envelopes and a weaker ISRF as the presumed Draine field, since the gas is only heated from the FUV component of the ISRF. Measuring the excitation of the gas in the envelopes is difficult, however, since the emission is weak, and most transitions are subthermally excited. The best-suited transition to study for this purpose might therefore be the $^{12}$CO ($J = 1{-}0$) line. Unfortunately, we do not have such data at hand. Another way to distinguish between both scenarios may be to study the distribution and emission of PAHs. All globules of this study have been mapped with *Spitzer's* infrared array camera (IRAC). In particular the 5.8 $\mu$m and 8 $\mu$m bands are known to show PAH emission (e.g., Pagani et al. 2010). However, the maps are not extended enough to define a background level that would allow absolute values of the emission to be derived.

#### 4.4.6. Constraints on the grain properties

To correctly model the observed molecular abundances, we must increase the molecular hydrogen density and, with it, the initial abundances of all species by a factor of 2 to 3 (except for B 68). We thus seem to systematically underestimate the hydrogen density in the dust-based modeling. This is understandable, at least in the envelopes of the cores, since we have assumed mildly coagulated grains, with a coagulation time of $10^5$ yr at a gas density of $10^5$ cm$^{-3}$ (Ossenkopf & Henning 1994)[8] over the entire globule. With the assumption of normal ISM dust (e.g., OH1), we would have derived hydrogen densities that are higher by a factor of 2.5. Increasing the density could also partly compensate for an underestimation of the gas temperature. However, we do not find any dependence on the observed $A_V$. Moreover, the only core for which we do not have to increase the density is that of B 68 – one of the least shielded cores in our sample. Our molecular line observations and modeling thus suggest that in most regions of the cores that are resolved by our study, the grains are not yet significantly coagulated.

[8] ftp://cdsarc.u-strasbg.fr/pub/cats/J/A+A/291/943

## 5. Conclusions

We observed a sample of seven globules containing starless cores in the $^{12}$CO ($J = 2{-}1$), the $^{13}$CO ($J = 2{-}1$), the C$^{18}$O ($J = 2{-}1$) and the $N_2H^+$ ($J = 1{-}0$) transitions. The globules were also observed with the *Herschel* bolometers as part of the EPoS project (Launhardt et al. 2013). We presented dust temperature and hydrogen density maps of the globules that were obtained with a ray-tracing technique. Based on these dust-based temperature and density profiles, we analyzed the molecular emission assuming $T_{Dust} = T_{Gas}$. In the following we summarize the main results of this study.

1. We confirm the findings of Launhardt et al. (2013) on the stability of the cores. Only one starless core (CB 244, see also Stutz et al. 2010) is clearly not supported against gravitational collapse by thermal pressure. CB 17, CB 27, and B 68 are probably also thermally supercritical. CB 4 and CB 26 are probably gravitationally stable.
2. CO is depleted in the center of all studied cores to a level of at least 46%. CB 27, B 68, and CB 244 show a central CO depletion of more than 90%. The level of freezeout increases towards the core centers and with the hydrogen density. The average radius at which half of the CO is frozen to the grains is 9000 AU, and the average hydrogen density is $10^5$ cm$^{-3}$.
3. $N_2H^+$ is depleted in the center of the cores with hydrogen densities exceeding $10^5$ cm$^{-3}$. The radius with maximum abundance of $N_2H^+$ is on average at 6800 AU. The degree of depletion in the center with respect to the maximum abundance ranges from 13% to 55%.
4. The chemical age at which we find that the models match the data best is higher for $^{13}$CO than for C$^{18}$O and $N_2H^+$. We find an average age of the six modeled cores of $2 \pm 1 \times 10^5$ yr for $^{13}$CO and of $6 \pm 3 \times 10^4$ yr for C$^{18}$O, and $9 \pm 2 \times 10^4$ yr for $N_2H^+$. The different ages of the dense gas tracers and $^{13}$CO suggest a central contraction of the cores during the chemical evolution. Considering the uncertainties, all cores have a chemical age of at most $10^6$ yr and are probably younger.
5. We generally need to increase the gas density that has been derived from the dust density, assuming mildly coagulated grains (OH5a) by a factor of 2–3 in order to model the observed molecular emission profiles correctly. We interpret this as a sign that the dust grains are not as heavily coagulated as assumed by our dust model in large parts of the globules and are better described by ISM dust models like OH1.
6. We have to reduce the strength of the UV radiation field impacting at the globule boundaries with respect to the value predicted by Draine (1978) for half of the cores. However, we think that this does not indicate that the impacting UV-field is in fact weaker, but rather that we thereby compensate for the systematic error that is introduced by the underestimation of the gas temperature in the envelopes of these cores.

*Acknowledgements.* We thank the anonymous referee and the editor M. Walmsley for comments and suggestions that helped to improve the clarity and completeness of the paper. We wish to thank the IRAM Granada staff for the

support at the 30 m telescope and T. Bergin for providing us with his line data of B 68. We also thank N. J. Evans II and E. Keto for interesting discussions that helped to improve the clarity of the paper. PACS has been developed by a consortium of institutes led by MPE (Germany), including UVIE (Austria); KU Leuven, CSL, IMEC (Belgium); CEA, LAM (France); MPIA (Germany); INAF-IFSI/OAA/OAP/OAT, LENS, SISSA (Italy); IAC (Spain). This development has been supported by the funding agencies BMVIT (Austria), ESA-PRODEX (Belgium), CEA/CNES (France), DLR (Germany), ASI/INAF (Italy), and CICYT/MCYT (Spain). The *Heinrich Hertz* Submillimeter Telescope is operated by Steward Observatory at the University of Arizona with partial support from the U.S. National Science Foundation through grant AST-1140030. D.S. acknowledges support by the Deutsche Forschungsgemeinschaft through SPP 1385: "The first ten million years of the solar system – a planetary materials approach" (SE 1962/1-1 and SE 1962/1-2). The work of A.M.S. was supported by the Deutsche Forschungsgemeinschaft priority program 1573 ("Physics of the Interstellar Medium"). Y.P. was supported by the Russian Foundation for Basic Research (project 13-02-00642). H.L., M.N., and Z.B. were funded by the Deutsches Zentrum für Luft- und Raumfahrt (DLR).

## References

Alves, F. O., & Franco, G. A. P. 2007, A&A, 470, 597
Alves, J. F., Lada, C. J., & Lada, E. A. 2001, Nature, 409, 159
Bacmann, A., Lefloch, B., Ceccarelli, C., et al. 2002, A&A, 389, L6
Bacmann, A., Taquet, V., Faure, A., Kahane, C., & Ceccarelli, C. 2012, A&A, 541, L12
Bergin, E. A., & Tafalla, M. 2007, ARA&A, 45, 339
Bergin, E. A., Alves, J., Huard, T., & Lada, C. J. 2002, ApJ, 570, L101
Bergin, E. A., Maret, S., van der Tak, F. F. S., et al. 2006, ApJ, 645, 369
Biham, O., Furman, I., Pirronello, V., & Vidali, G. 2001, ApJ, 553, 595
Bonnor, W. B. 1956, MNRAS, 116, 351
Brinch, C., & Hogerheijde, M. R. 2010, A&A, 523, A25
Carter, M., Lazareff, B., Maier, D., et al. 2012, A&A, 538, A89
Caselli, P., Myers, P. C., & Thaddeus, P. 1995, ApJ, 455, L77
Caselli, P., Walmsley, C. M., Tafalla, M., Dore, L., & Myers, P. C. 1999, ApJ, 523, L165
de Geus, E. J., de Zeeuw, P. T., & Lub, J. 1989, A&A, 216, 44
Draine, B. T. 1978, ApJS, 36, 595
Draine, B. T., & Bertoldi, F. 1996, ApJ, 468, 269
Ebert, R. 1955, ZAp, 37, 217
Evans, II, N. J., Rawlings, J. M. C., Shirley, Y. L., & Mundy, L. G. 2001, ApJ, 557, 193
Ford, A. B., & Shirley, Y. L. 2011, ApJ, 728, 144
Galli, D., Walmsley, M., & Gonçalves, J. 2002, A&A, 394, 275
Garrod, R. T. 2013, ApJ, 765, 60
Garrod, R. T., & Herbst, E. 2006, A&A, 457, 927
Garrod, R. T., Wakelam, V., & Herbst, E. 2007, A&A, 467, 1103
Griffin, M. J., Abergel, A., Abreu, A., et al. 2010, A&A, 518, L3
Herbst, E., & Klemperer, W. 1973, ApJ, 185, 505
Hotzel, S., Harju, J., Juvela, M., Mattila, K., & Haikala, L. K. 2002, A&A, 391, 275
Indriolo, N., Neufeld, D. A., Gerin, M., et al. 2012, ApJ, 758, 83
Kainulainen, J., Lehtinen, K., & Harju, J. 2006, A&A, 447, 597
Katz, N., Furman, I., Biham, O., Pirronello, V., & Vidali, G. 1999, ApJ, 522, 305
Keto, E., & Caselli, P. 2008, ApJ, 683, 238
Kun, M. 1998, ApJS, 115, 59
Lai, S.-P., Velusamy, T., Langer, W. D., & Kuiper, T. B. H. 2003, AJ, 126, 311
Langer, W. D., Graedel, T. E., Frerking, M. A., & Armentrout, P. B. 1984, ApJ, 277, 581
Launhardt, R., & Henning, T. 1997, A&A, 326, 329
Launhardt, R., & Sargent, A. I. 2001, ApJ, 562, L173
Launhardt, R., Nutter, D., Ward-Thompson, D., et al. 2010, ApJS, 188, 139
Launhardt, R., Stutz, A. M., Schmiedeke, A., et al. 2013, A&A, 551, A98
Lee, C. W., & Myers, P. C. 1999, ApJS, 123, 233
Lee, H.-H., Herbst, E., Pineau des Forets, G., Roueff, E., & Le Bourlot, J. 1996, A&A, 311, 690
Lee, J.-E., Evans, II, N. J., Shirley, Y. L., & Tatematsu, K. 2003, ApJ, 583, 789
Lodders, K., Palme, H., & Gail, H.-P. 2009, Landolt Börnstein, 44
Loinard, L., Mioduszewski, A. J., Torres, R. M., et al. 2011, Rev. Mex. Astron. Astrofis. Conf. Ser., 40, 205
Lombardi, M., Alves, J., & Lada, C. J. 2006, A&A, 454, 781
Miville-Deschênes, M.-A., & Lagache, G. 2005, ApJS, 157, 302
Nielbock, M., Launhardt, R., Steinacker, J., et al. 2012, A&A, 547, A11
Öberg, K. I., Linnartz, H., Visser, R., & van Dishoeck, E. F. 2009a, ApJ, 693, 1209
Öberg, K. I., van Dishoeck, E. F., & Linnartz, H. 2009b, A&A, 496, 281
Ossenkopf, V., & Henning, T. 1994, A&A, 291, 943
Pagani, L., Pardo, J.-R., Apponi, A. J., Bacmann, A., & Cabrit, S. 2005, A&A, 429, 181
Pagani, L., Steinacker, J., Bacmann, A., Stutz, A., & Henning, T. 2010, Science, 329, 1622
Pavlyuchenkov, Y., Wiebe, D., Launhardt, R., & Henning, T. 2006, ApJ, 645, 1212
Pavlyuchenkov, Y., Henning, T., & Wiebe, D. 2007, ApJ, 669, L101
Perrot, C. A., & Grenier, I. A. 2003, A&A, 404, 519
Pickett, H. M., Poynter, R. L., Cohen, E. A., et al. 1998, J. Quant. Spectr. Rad. Transf., 60, 883
Pilbratt, G. L., Riedinger, J. R., Passvogel, T., et al. 2010, A&A, 518, L1
Plummer, H. C. 1911, MNRAS, 71, 460
Poglitsch, A., Waelkens, C., Geis, N., et al. 2010, A&A, 518, L2
Schmalzl, M., Launhardt, R., Stutz, A. M., et al. 2013, A&A, submitted
Schöier, F. L., van der Tak, F. F. S., van Dishoeck, E. F., & Black, J. H. 2005, A&A, 432, 369
Semenov, D., Hersant, F., Wakelam, V., et al. 2010, A&A, 522, A42
Shalabiea, O. M., & Greenberg, J. M. 1994, A&A, 290, 266
Stahler, S. W., & Palla, F. 2005, The Formation of Stars (Wiley-VCH)
Straižys, V., Černis, K., & Bartašiūtė, S. 2003, A&A, 405, 585
Stutz, A. M., Rieke, G. H., Bieging, J. H., et al. 2009, ApJ, 707, 137
Stutz, A., Launhardt, R., Linz, H., et al. 2010, A&A, 518, L87
Tafalla, M., & Santiago, J. 2004, A&A, 414, L53
Tafalla, M., Myers, P. C., Caselli, P., Walmsley, C. M., & Comito, C. 2002, ApJ, 569, 815
Tafalla, M., Myers, P. C., Caselli, P., & Walmsley, C. M. 2004, A&A, 416, 191
Tielens, A. G. G. M., Tokunaga, A. T., Geballe, T. R., & Baas, F. 1991, ApJ, 381, 181
van der Tak, F. F. S., Black, J. H., Schöier, F. L., Jansen, D. J., & van Dishoeck, E. F. 2007, A&A, 468, 627
van Dishoeck, E. F., Jonkheid, B., & van Hemert, M. C. 2006, Chemical evolution of the Universe, Faraday discussions, 133, 231
Vasyunin, A. I., & Herbst, E. 2013, ApJ, 769, 34
Whitworth, A. P., & Ward-Thompson, D. 2001, ApJ, 547, 317
Willacy, K., Langer, W. D., & Velusamy, T. 1998, ApJ, 507, L171
Willacy, K., Langer, W. D., & Allen, M. 2002, ApJ, 573, L119
Wilson, T. L., & Rood, R. 1994, ARA&A, 32, 191
Witt, A. N., Oliveri, M. V., & Schild, R. E. 1990, AJ, 99, 888
Wolf, S., Launhardt, R., & Henning, T. 2003, ApJ, 592, 233
Xie, T., Allen, M., & Langer, W. D. 1995, ApJ, 440, 674

Pages 17 to 24 are available in the electronic edition of the journal at http://www.aanda.org

## Appendix A: Observations

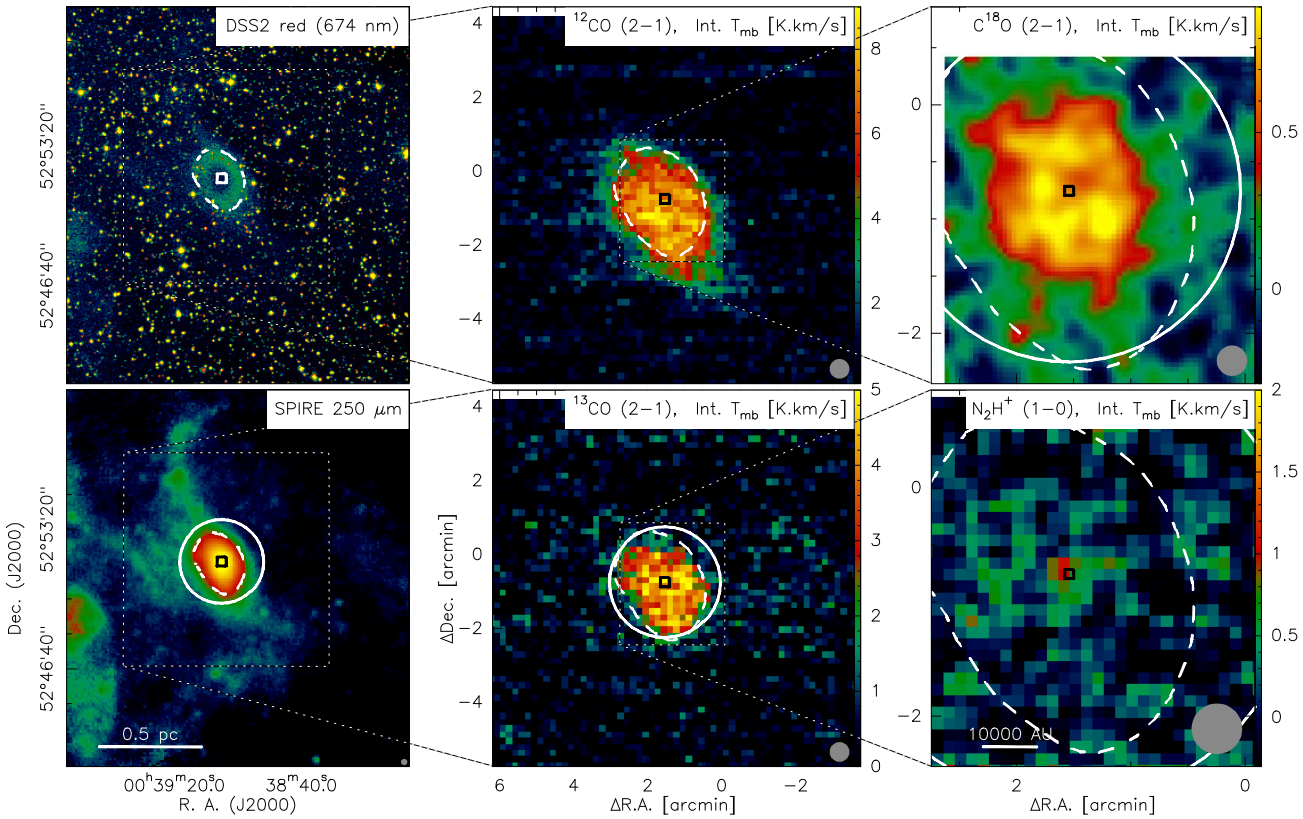


**Fig. A.1.** Observations of CB4. Digitized Sky Survey (DSS) red, *Herschel* SPIRE 250 $\mu$m, $^{12}$CO ($J$ = 2−1), $^{13}$CO ($J$ = 2−1), $C^{18}O$ ($J$ = 2−1), and $N_2H^+$ ($J$ = 1−0). The gray circles in the lower right corners indicate the respective beam sizes. The square marker indicates the center of the starless core. The dashed contour marks $N_H = 10^{21}$ cm$^{-2}$. The white circles indicate the regions of which 1D-profiles were obtained by azimuthally averaging.

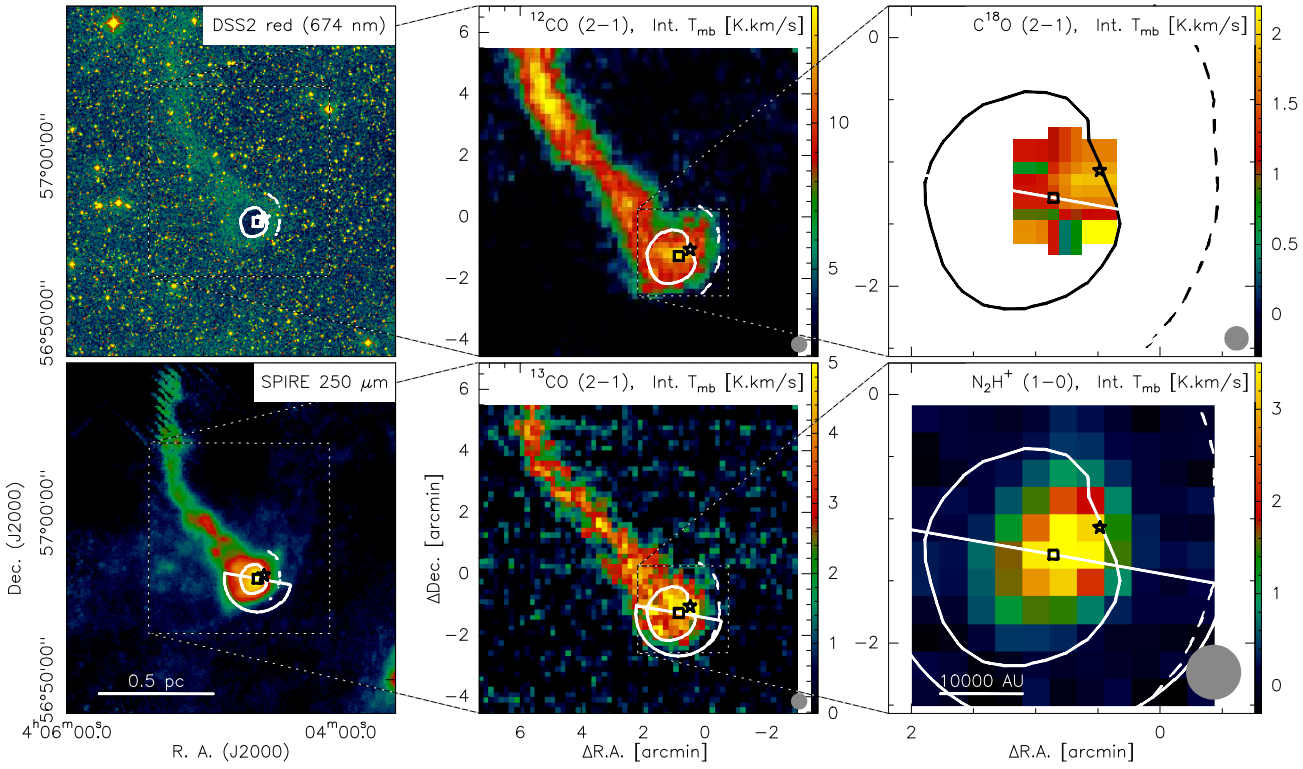


**Fig. A.2.** Observations of CB17. DSS red, *Herschel* SPIRE 250 $\mu$m, $^{12}$CO ($J$ = 2−1), $^{13}$CO ($J$ = 2−1), $C^{18}O$ ($J$ = 2−1), and $N_2H^+$ ($J$ = 1−0). The gray circles in the lower right corners indicate the respective beam sizes. The square marker indicates the center of the starless core, the asterisk the position of the Class I YSO. The dashed contour marks $N_H = 10^{21}$ cm$^{-2}$, the solid contour $N_H = 10^{22}$ cm$^{-2}$. The white circles indicate the regions where 1D-profiles were obtained by azimuthally averaging.

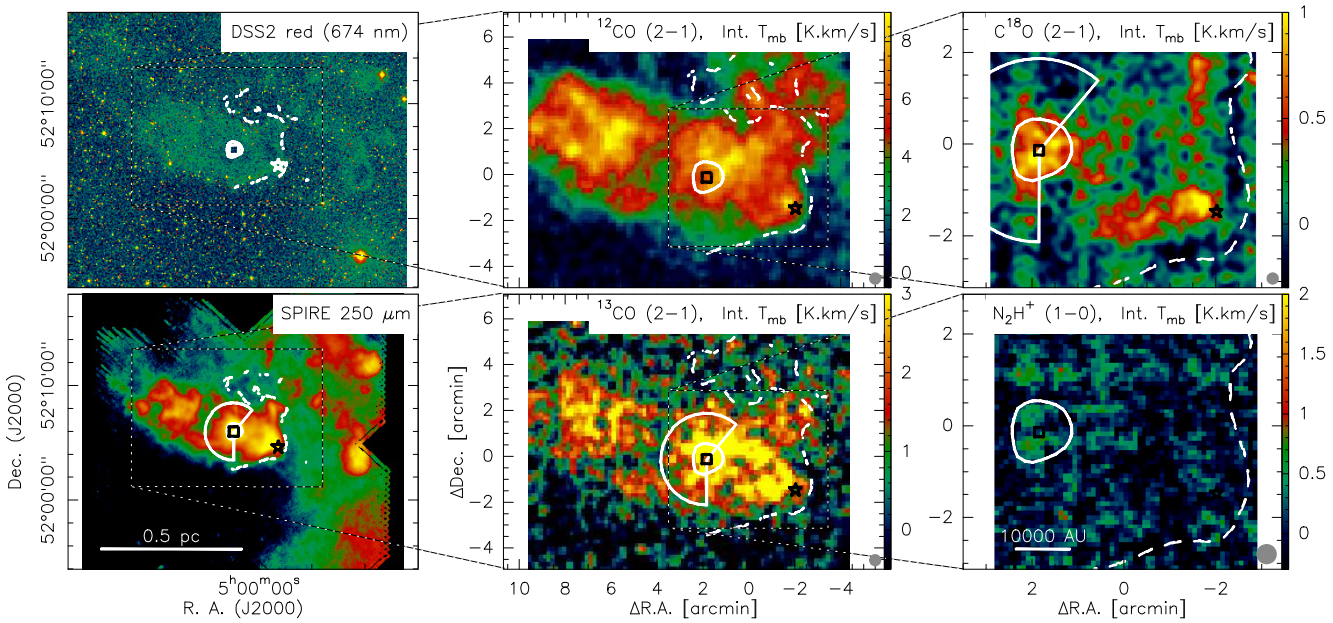


**Fig. A.3.** Observations of CB26. DSS red, *Herschel* SPIRE 250 $\mu$m, $^{12}$CO ($J$ = 2−1), $^{13}$CO ($J$ = 2−1), $C^{18}O$ ($J$ = 2−1), and $N_2H^+$ ($J$ = 1−0). The gray circles in the lower right corners indicate the respective beam sizes. The square marker indicates the center of the starless core, the asterisk the position of the Class I YSO. The dashed contour marks $N_H = 10^{21}$ cm$^{-2}$, the solid contour $N_H = 10^{22}$ cm$^{-2}$. The white circles indicate the regions where 1D-profiles were obtained by azimuthally averaging.

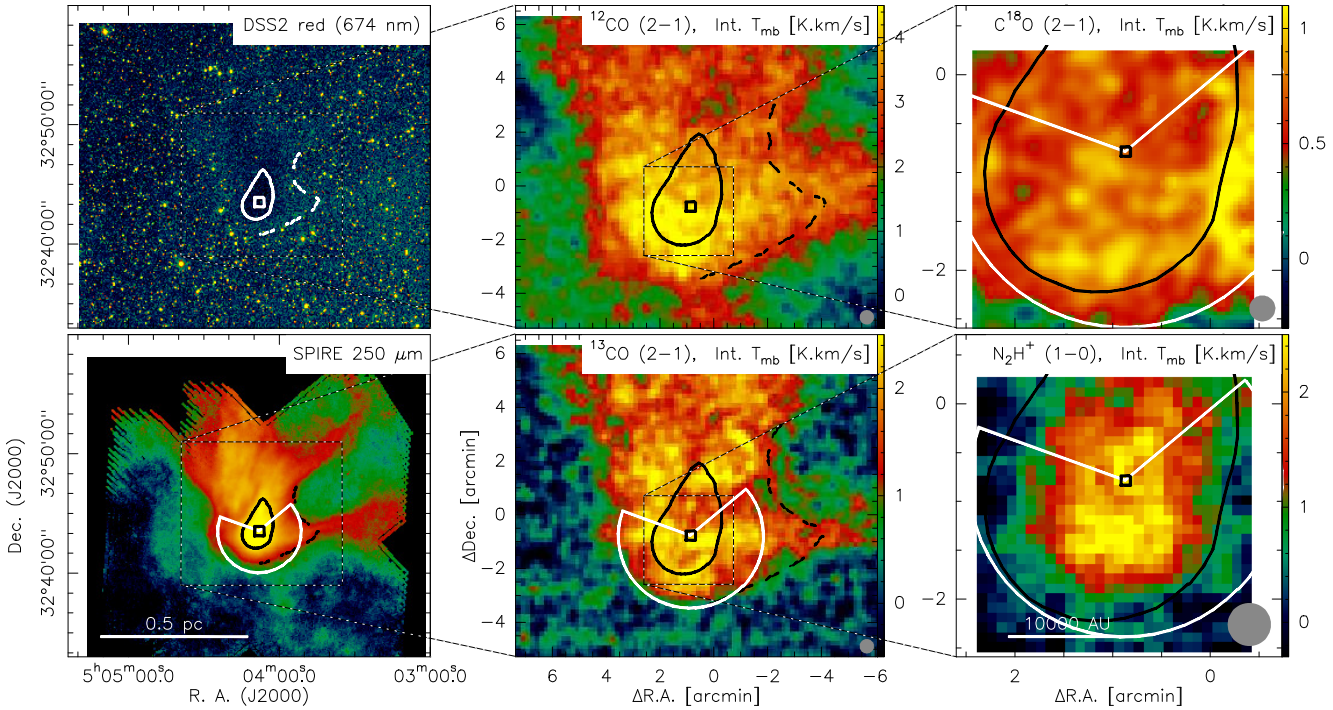


**Fig. A.4.** Observations of CB27. DSS red, *Herschel* SPIRE 250 $\mu$m, $^{12}$CO ($J$ = 2−1), $^{13}$CO ($J$ = 2−1), $C^{18}O$ ($J$ = 2−1), and $N_2H^+$ ($J$ = 1−0). The gray circles in the lower right corners indicate the respective beam sizes. The square marker indicates the center of the starless core. The dashed contour marks $N_H = 10^{21}$ cm$^{-2}$, the solid contour $N_H = 10^{22}$ cm$^{-2}$. The white circles indicate the regions where 1D-profiles were obtained by azimuthally averaging.

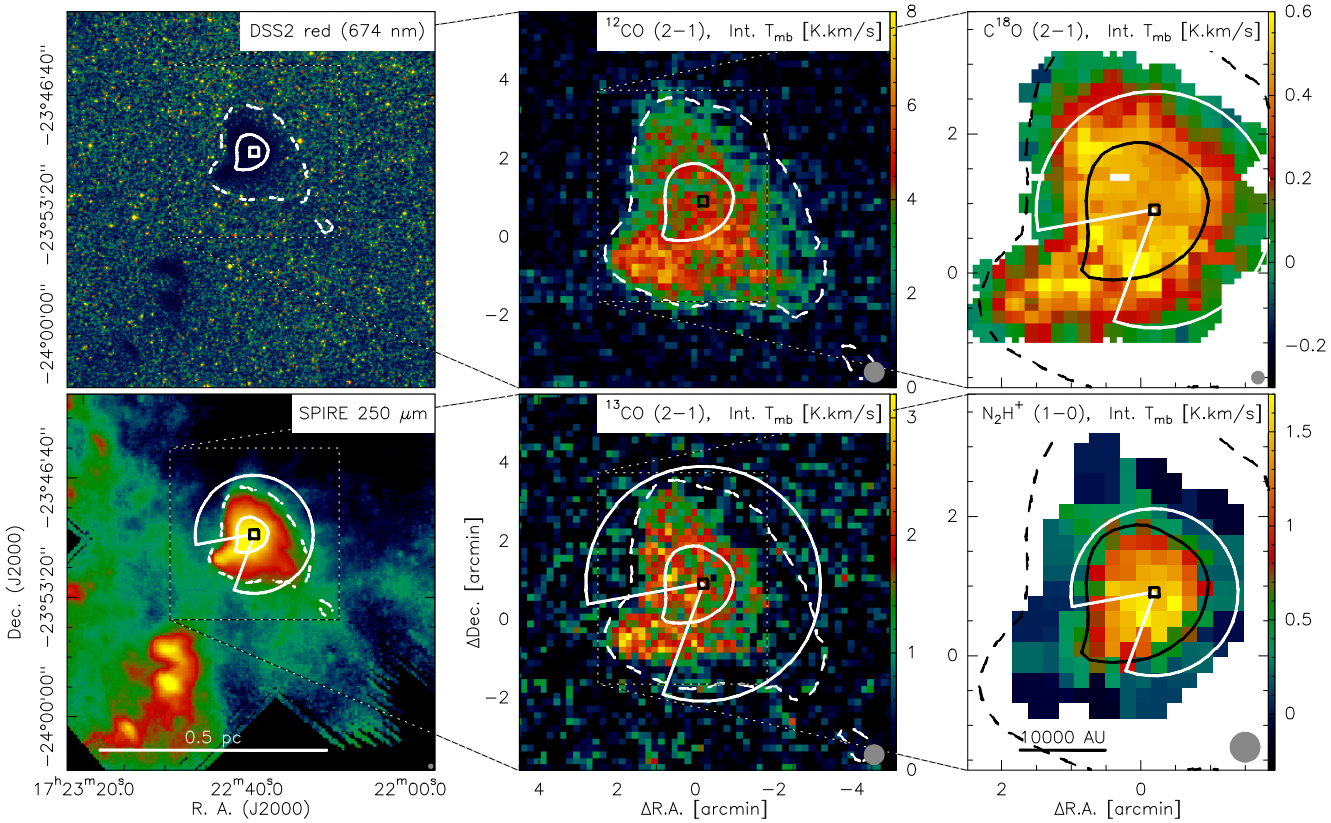


**Fig. A.5.** Observations of B68. DSS red, *Herschel* SPIRE 250 $\mu$m, $^{12}$CO ($J$ = 2−1), $^{13}$CO ($J$ = 2−1), C$^{18}$O ($J$ = 2−1), and $N_2H^+$ ($J$ = 1−0). The gray circles in the lower right corners indicate the respective beam sizes. The square marker indicates the center of the starless core. The dashed contour marks $N_H = 10^{21}$ cm$^{-2}$, the solid contour $N_H = 10^{22}$ cm$^{-2}$. The white circles indicate the regions where 1D-profiles were obtained by azimuthally averaging.

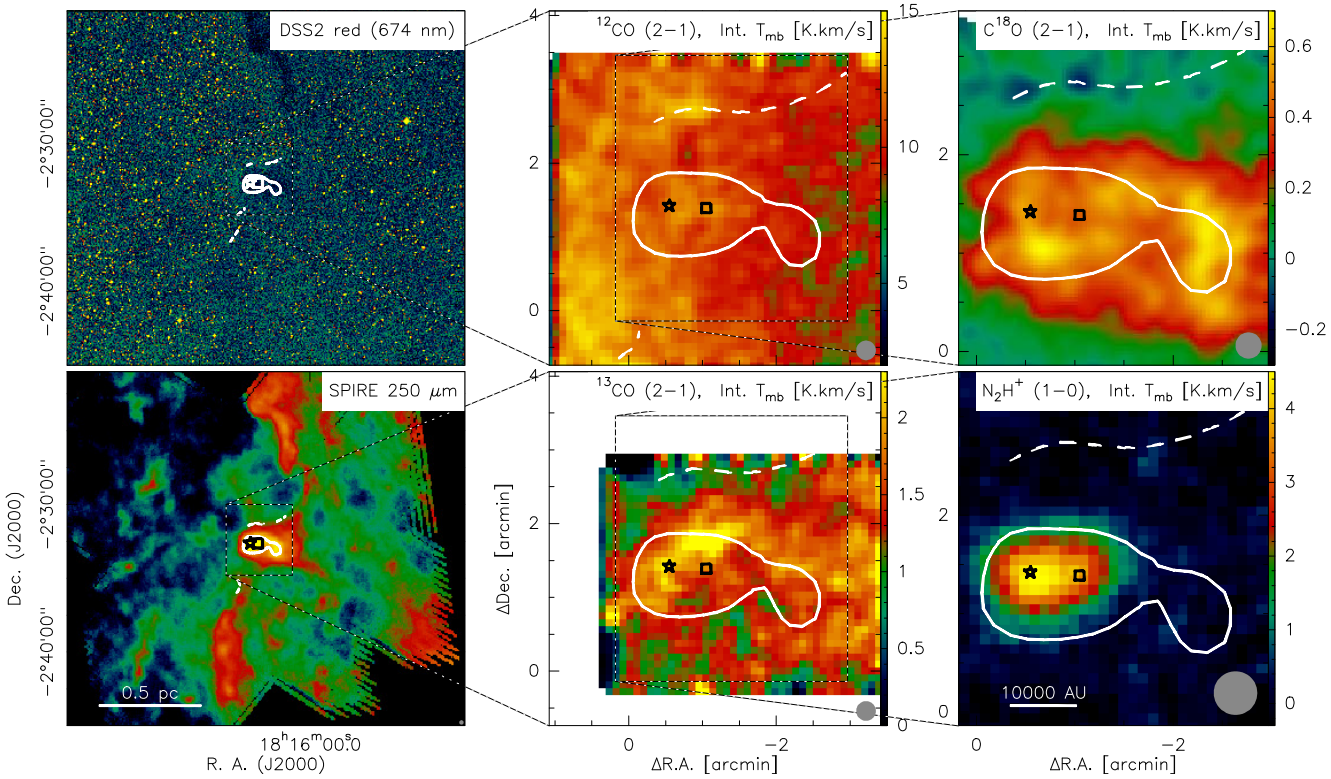


**Fig. A.6.** Observations of CB130: DSS red, *Herschel* SPIRE 250 $\mu$m, $^{12}$CO ($J$ = 2−1), $^{13}$CO ($J$ = 2−1), C$^{18}$O ($J$ = 2−1), and $N_2H^+$ ($J$ = 1−0). The gray circles in the lower right corners indicate the respective beam sizes. The square marker indicates the center of the starless core, the asterisk the position of the Class I YSO. The dashed contour marks $N_H = 10^{21}$ cm$^{-2}$, the solid contour $N_H = 10^{22}$ cm$^{-2}$. The white circles indicate the regions where 1D-profiles were obtained by azimuthally averaging.

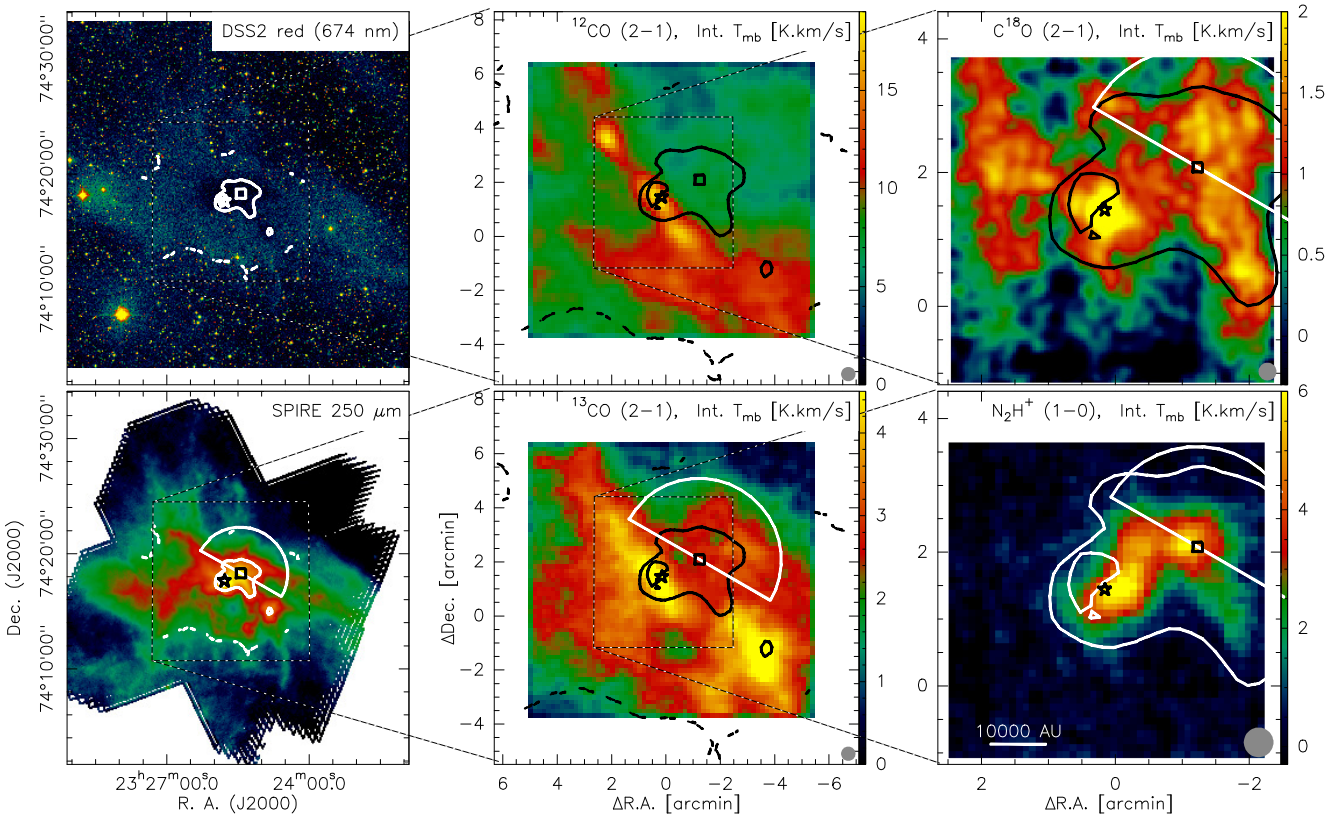


**Fig. A.7.** Observations of CB244: DSS red, *Herschel* SPIRE 250 $\mu$m, $^{12}$CO ($J$ = 2–1), $^{13}$CO ($J$ = 2–1), C$^{18}$O ($J$ = 2–1), and $N_2H^+$ ($J$ = 1–0). The gray circles in the lower right corners indicate the respective beam sizes. The square marker indicates the center of the starless core, the asterisk the center of the Class 0 protostellar core. The dashed contour marks $N_H = 10^{21}$ cm$^{-2}$, the solid contour $N_H = 10^{22}$ cm$^{-2}$. The white circles indicate the regions where 1D-profiles were obtained by azimuthally averaging.

## Appendix B: Hydrogen density and dust temperature maps

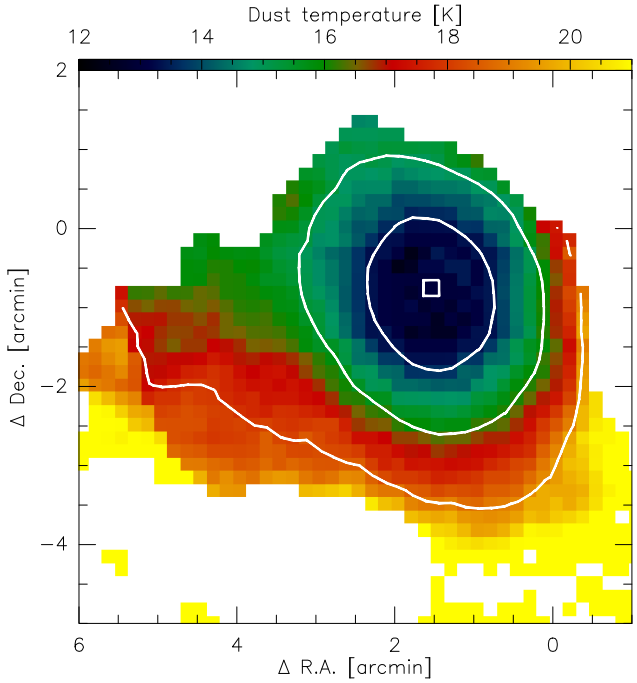


**Fig. B.1.** Dust temperature map of CB4 overlaid with contours of the hydrogen density. They mark densities of $10^2$, $10^3$, and $10^4$ cm$^{-3}$. The square indicates the center of the starless core.

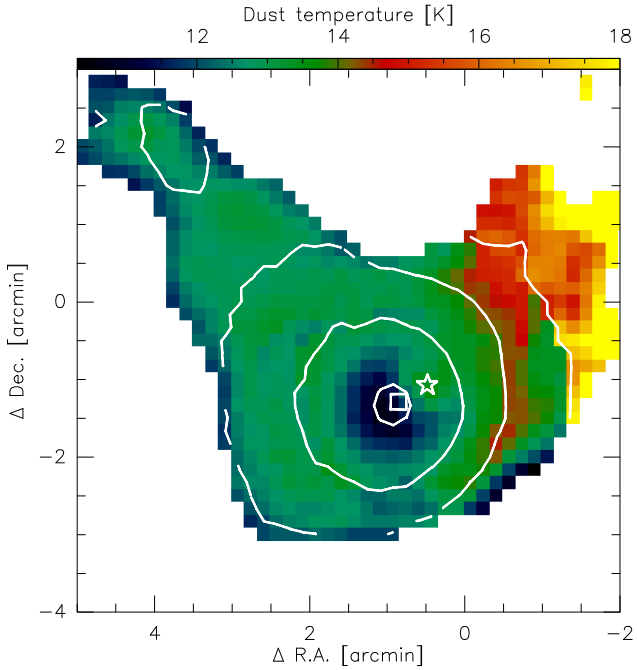


**Fig. B.2.** Dust temperature map of CB17 overlaid with contours of the hydrogen density. They mark densities of $10^2$, $10^3$, $10^4$, and $10^5$ cm$^{-3}$. The square indicates the center of the starless core.

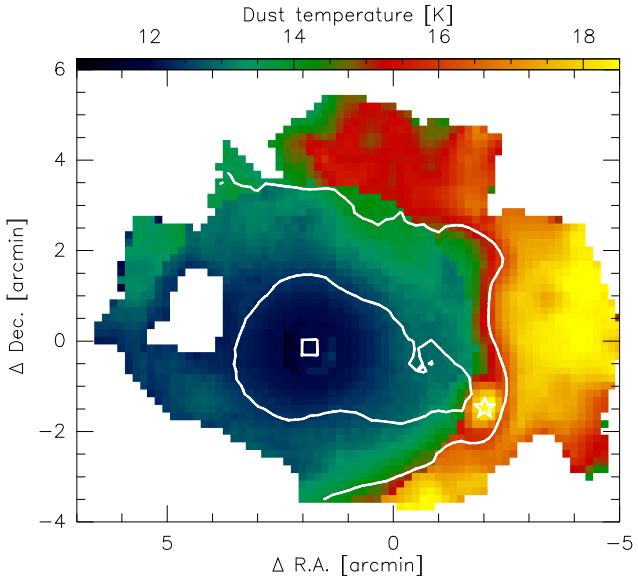


**Fig. B.3.** Dust temperature map of CB26 overlaid with contours of the hydrogen density. They mark densities of $10^3$, and $10^4$ cm$^{-3}$. The square indicates the center of the starless core.

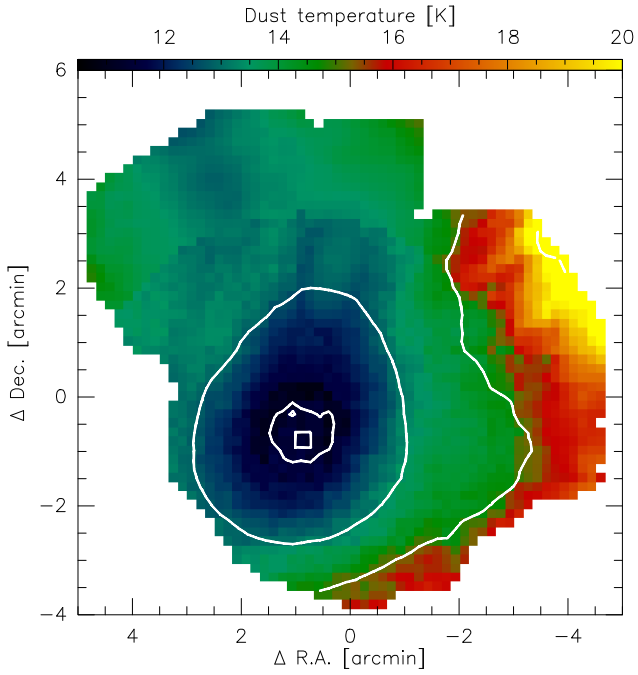


**Fig. B.4.** Dust temperature map of CB27 overlaid with contours of the hydrogen density. They mark densities of $10^3$, $10^4$, and $10^5$ cm$^{-3}$. The square indicates the center of the starless core.

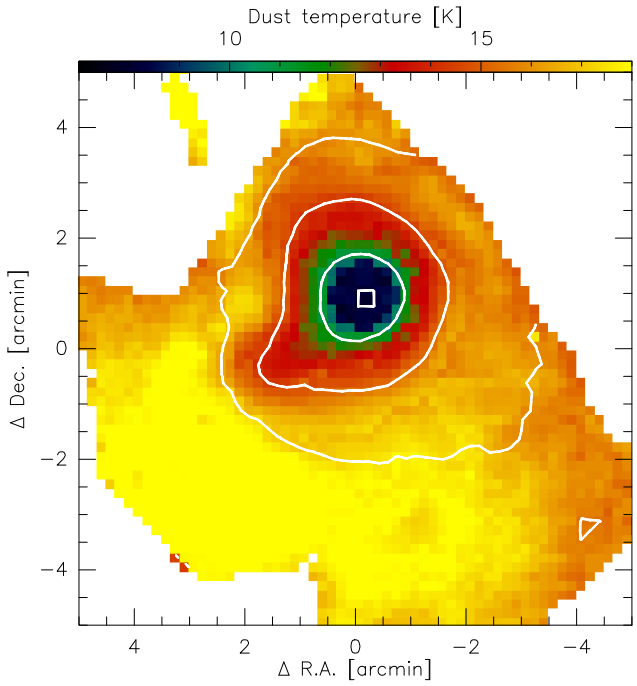


**Fig. B.5.** Dust temperature map of B68 overlaid with contours of the hydrogen density. They mark densities of $10^3$, $10^4$, and $10^5$ cm$^{-3}$. The square indicates the center of the starless core.

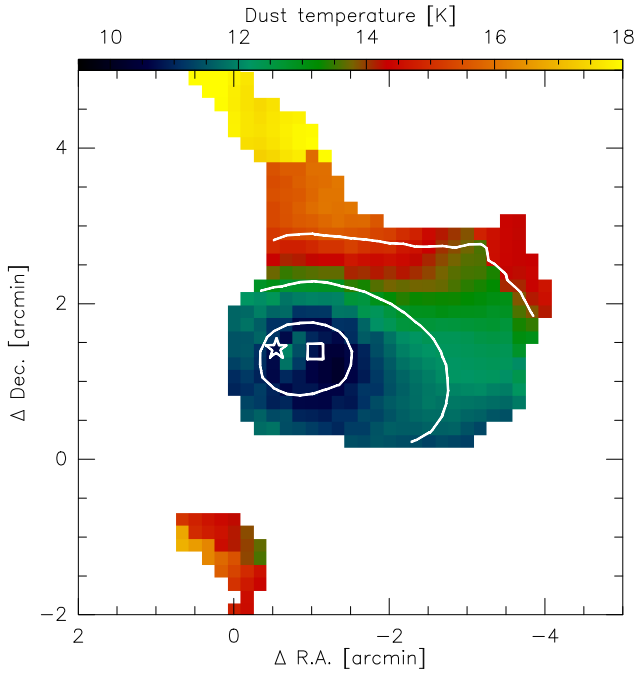


**Fig. B.6.** Dust temperature map of CB130 overlaid with contours of the hydrogen density. They mark densities of $10^3$, $10^4$, and $10^5$ cm$^{-3}$. The square indicates the center of the starless core.

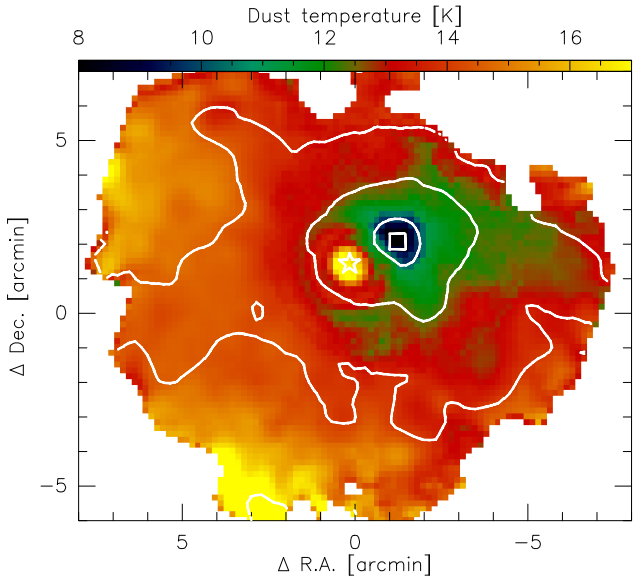


**Fig. B.7.** Dust temperature map of CB244 overlaid with contours of the hydrogen density. They mark densities of $10^3$, $10^4$, and $10^5$ cm$^{-3}$. The square indicates the center of the starless core.

## Appendix C: LTE Analysis

### C.1. Model

We estimated the molecular column densities of $^{13}$CO, C$^{18}$O, and $N_2H^+$ in a first step with a simple and well-established approach. For completeness, we briefly describe here this simplified approach and the results and discuss the differences and drawbacks with respect to the full chemical modeling.

We do not model the emission of the $^{12}$CO ($J$ = 2−1) transition, since it becomes optically thick already at $n_H < 10^4$ and therefore does not trace the regions of expected freezeout. At these low densities, gas and dust temperatures might also be decoupled (Galli et al. 2002), which is an additional obstacle for interpreting the $^{12}$CO emission.

The method is described in Stahler & Palla (2005). It assumes LTE and a constant gas temperature along the LoS. Since we do not have an independent measurement of the gas temperature, we make the simplifying assumption that the kinetic gas temperature is the same as the dust temperature we obtained from the LoS-averaged black-body-fitting of the continuum data in Launhardt et al. (2013). This is justified in the dense interiors of the starless cores, but may no longer be strictly valid in the outer parts at hydrogen densities below a few $10^4$ cm$^{-3}$.

To prepare the analysis, we obtain maps of the flux in the observed lines by integrating over the velocity axis of the spectral cubes. Maps of the linewidths of the CO isotopologues were derived from Gaussian fits to the spectra. For $N_2H^+$ we use the hfs-fitting routine provided with the *CLASS* package of *GILDAS*[9]. This routine allows fitting the full hyperfine structure of the $J$ = 1−0 transition and thus also derives the optical depth of the lines. The frequency offsets and relative strengths of the individual lines are adopted from Caselli et al. (1995). With these intermediate results at hand we can derive the molecular column densities using

$$N = \frac{8\pi\nu_0^2\Delta\nu Q\Delta\tau}{c^2 A_{\rm ul}}\left(\frac{g_{\rm l}}{g_{\rm u}}\right)\left[1-\exp\left(-\frac{T_0}{T_{\rm ex}}\right)\right]^{-1}, \tag{C.1}$$

where $\nu_0$ is the frequency of the transition, $\Delta\nu$ the observed linewidth, $Q$ the partition function of the rotational levels, $\Delta\tau$ the total optical thickness of the line, $A_{\rm ul}$ the Einstein parameter of the transition, $g_i$ the relative statistical weights of the upper and lower levels, $T_0 = h\nu_0/k_{\rm B}$, and $T_{\rm ex}$ the excitation temperature of the molecules. Since we assume LTE, we set $T_{\rm ex} = T_{\rm gas} = T_{\rm dust,\,MBB}$. The partition function $Q$ is given by

$$Q = \sum_J (2J+1)\exp\left[-\frac{h}{k_{\rm B}T_{\rm ex}}(BJ(J+1))\right], \tag{C.2}$$

where $B$ = 55 101.011 MHz is the rotational constant for $^{13}$CO, $B$ = 54 891.420 MHz for C$^{18}$O, and $B$ = 46 586.867 MHz for $N_2H^+$ (Pickett et al. 1998). While the optical depth of $N_2H^+$ could be determined directly by comparing the strength of the individual hyperfine components, we need to apply the "detection equation" in order to derive the optical depth of the CO lines:

$$T_B = T_0\left[f(T_{\rm ex}) - f(T_{\rm bg})\right]\left[1-{\rm e}^{-\Delta\tau}\right], \tag{C.3}$$

where $f(T) \equiv (\exp(T_0/T)-1)^{-1}$, $T_{\rm bg}$ = 2.73 K, and $T_B$ taken as the peak value of the Gaussian fits.

One-dimensional profiles of the resulting maps were obtained by azimuthally averaging around the core centers. In case of asymmetries, a segment of the circle in this direction has been masked for the averaging task. The regions that have been taken into account for deriving the 1D-profiles are indicated in Figs. A.1–A.7.

### C.2. Results

The derived radial profiles of the molecular column densities of $^{13}$CO, C$^{18}$O ,and $N_2H^+$ are presented in Fig. C.1. We find signs of depletion of $^{13}$CO in all cores except for CB 4, which is the most tenuous core of the studied sample. The $^{13}$CO column density of the other cores decreases constantly with the increasing hydrogen column density. The results for $^{13}$CO are, however, affected by optical depth effects, as well as deviations of the gas temperature from the LoS-averaged dust temperature and subthermal rotational excitation.

The derivation of C$^{18}$O column densities is less influenced by these effects since it is a rarer isotopologue (a factor of ∼7 lower abundance as compared to $^{13}$CO) and since its emission comes from more restricted regions with higher gas densities. The plots of the $^{13}$CO column densities vs. visual extinction (top left panel of Fig. C.1) yield a remarkable difference to those of the C$^{18}$O column densities. The relative abundance of $^{13}$CO drops continuously with increasing extinction, indicating central depletion of this species. While this behavior is also found for C$^{18}$O, its relative abundance also drops toward low hydrogen column densities and peaks between an $A_v$ of 5 to 10 mag. The drop toward lower extinction can be explained by a weaker self-shielding of this rare isotopologue, which in turn leads to photodissociation of C$^{18}$O in the envelopes where $^{13}$CO is already well shielded. The chemical modeling, however, suggests that the UV radiation is already attenuated by several magnitudes in these regions compared to the nominal strength of the ISRF (see Sect. 4.4.5). The difference in the profiles of both species becomes more obvious from the ratio of both column densities. The ratio $N(^{13}{\rm CO})/N({\rm C}^{18}{\rm O})$ decreases continuously with increasing hydrogen column density in all starless cores. Interestingly, it even drops below the usually assumed ratio of 7 for the ISM. The change in the $N(^{13}{\rm CO})/N({\rm C}^{18}{\rm O})$ ratio could thus not only be due to different self-shielding of both species but also partly due to reactions that increase the abundance of C$^{18}$O with respect to $^{13}$CO due to ion-molecule exchange reactions in cold and dense environments (e.g., Langer et al. 1984).

Where the $N_2H^+$ emission is strong enough to fit the hyperfine structure, we also derive column densities for this molecule. We find that the ratio $N(N_2H^+)/N_{\rm H}$ is roughly constant within the globules (see bottom row of Fig. C.1). This finding contrasts with the results of our advanced approach using chemical modeling and a subsequent line-radiative transfer. There we find depletion of $N_2H^+$ in the centers of the majority of the globules (see Sect. 4.4.3 and Fig. 6). This demonstrates the limitation of the often-used LOS-averaged analysis.

[9] http://www.iram.fr/IRAMFR/GILDAS

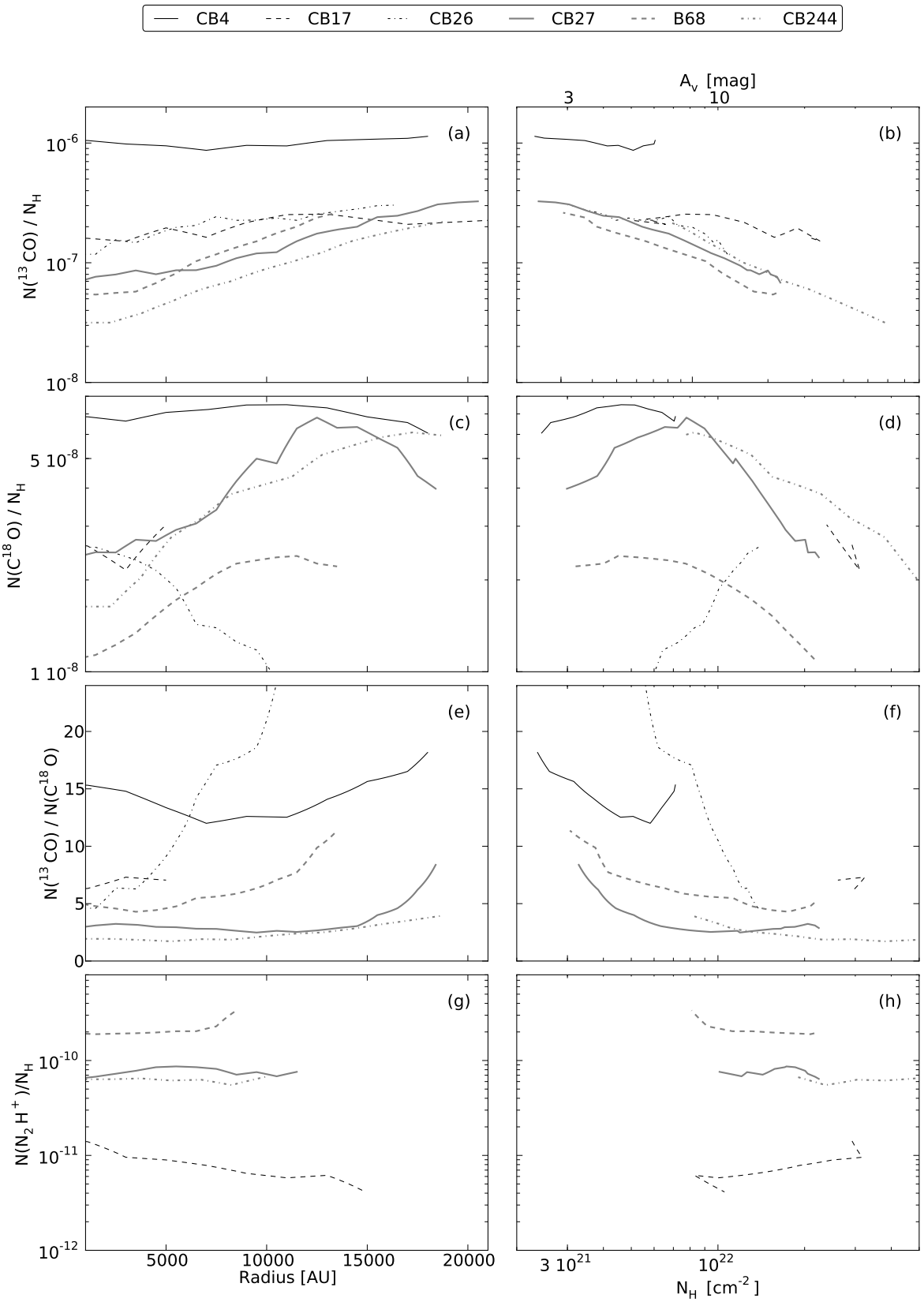


**Fig. C.1.** Results from the LTE-analysis. Plotted are **a)** the relative column densities of $^{13}$CO against radius **b)** and against the hydrogen column density, **c)** the relative column densities of C$^{18}$O against radius **d)** and against the hydrogen column density, **e)** the ratios of $N(^{13}\mathrm{CO})/N(\mathrm{C}^{18}\mathrm{O})$ are plotted against radius **f)** and against the hydrogen column density, **g)** the relative column densities of $N_2H^+$against radius, **h)** and against the hydrogen column density. The column densities of $N_2H^+$ in CB 4 and CB 26 could not be derived, since the emission in these globules is too weak and so are missing in the plots.